Cell Reports

Article

A neurogenic microenvironment defined by excitatory-inhibitory neuronal circuits in adult dentate gyrus

Graphical abstract

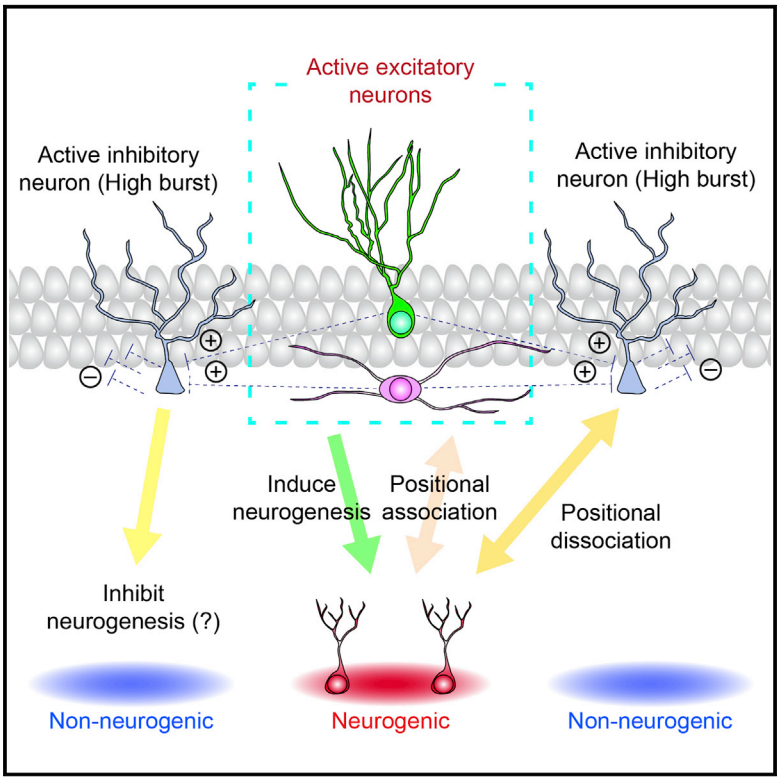

Highlights

- Neurogenesis and place cells are anatomically associated in the adult dentate gyrus
- Neurogenesis and interneurons are anatomically dissociated in the adult dentate gyrus
- A subset of interneurons receives synaptic activation from excitatory neurons nearby
- Brief optogenetic activation of excitatory neurons stimulates adult neurogenesis

Authors

Masato Uemura, Stefan Blankvoort, Sean Shui Liang Tok, Li Yuan, Luis Fernando Cobar, Kwok Keung Lit, Ayumu Tashiro

Correspondence

atashiro@ntu.edu.sg

In brief

Uemura et al. show that neurogenesis is anatomically associated with place-cell activity and dissociated from a type of active interneuron in the adult dentate gyrus. Increased neurogenesis resulting from optogenetic activation of excitatory circuits indicates that this association may be caused by local activity-dependent stimulation of neurogenesis.

Uemura et al., 2021, Cell Reports *36*, 109324
July 6, 2021
https://doi.org/10.1016/j.celrep.2021.109324

CellPress

Cell Reports

CellPress
OPEN ACCESS

Article

A neurogenic microenvironment defined by excitatory-inhibitory neuronal circuits in adult dentate gyrus

Masato Uemura,[1,3,4] Stefan Blankvoort,[1,3] Sean Shui Liang Tok,[2] Li Yuan,[2] Luis Fernando Cobar,[2] Kwok Keung Lit,[2] and Ayumu Tashiro[1,2,5,*]

[1]Kavli Institute for Systems Neuroscience, Norwegian University of Science and Technology, 7030 Trondheim, Norway
[2]School of Biological Sciences, Nanyang Technological University, Singapore 308232, Singapore
[3]These authors contributed equally
[4]Present address: Department of Biology, Kansai Medical University, Hirakata, Osaka 573-1010, Japan
[5]Lead contact
*Correspondence: atashiro@ntu.edu.sg
https://doi.org/10.1016/j.celrep.2021.109324

SUMMARY

Adult neurogenesis in the dentate gyrus plays a role in adaptive brain functions such as memory formation. Adding new neurons to a specific locus of a neural circuit with functional needs is an efficient way to achieve such an adaptive function. However, it is unknown whether neurogenesis is linked to local functional demands potentially specified by the activity of neuronal circuits. By examining the distribution of neurogenesis and different types of neuronal activity in the dentate gyrus of freely moving adult rats, we find that neurogenesis is positionally associated with active excitatory neurons, some of which show place-cell activity, but is positionally dissociated from a type of interneuron with high-burst tendency. Our finding suggests that the behaviorally relevant activity of excitatory-inhibitory neuronal circuits can define a microenvironment stimulating/inhibiting neurogenesis. Such local regulation of neurogenesis may contribute to strategic recruitment of new neurons to modify functionally relevant neural circuits.

INTRODUCTION

After the completion of the major period of neurogenesis in embryonic stages, neurogenesis continues in limited regions in the mammalian brain and works as a form of adaptive brain plasticity to meet environmental demands (Christian et al., 2014; Deng et al., 2010; Kempermann, 2012). One such region is the dentate gyrus, where a principal neuronal type, granule cells, is generated. Newly generated granule cells go through a series of maturation processes, including neurite extension, synapse formation, and selection for survival or death (Biebl et al., 2000; Zhao et al., 2006). These maturation processes depend on activity (Bruel-Jungerman et al., 2006; Deisseroth et al., 2004; Derrick et al., 2000; Ge et al., 2006; Gould et al., 1997; Stone et al., 2011; Tashiro et al., 2006) and experience (Aasebø et al., 2018; Bergami et al., 2015; Döbrössy et al., 2003; Gould et al., 1999; Kempermann et al., 1997; Tashiro et al., 2007; van Praag et al., 1999). The modification of neural circuits resulting from the addition of new neurons is thought to reflect the animal's experience and contribute to adaptive brain functions (Aasebø et al., 2011).

During embryonic and early postnatal development, large numbers of newborn neurons are distributed all over the dentate gyrus and are available for modifying circuits (with some regional variation) (Snyder et al., 2009b). The rate of neuronal birth exponentially decreases along the animal's age, limiting the availability of new neurons (Kuhn et al., 1996). For example, in such situations that happen in the adult and/or juvenile human brain (Moreno-Jiménez et al., 2019; Sorrells et al., 2018), the system would be extremely inefficient if neuronal birth occurs randomly without reflecting functional needs. Instead, the benefit of newly generated neurons can be maximized if they are recruited to loci with functional needs for circuit modification. Previous studies have established that the amount of neuronal birth is regulated based on experience (Gould et al., 1997; van Praag et al., 1999) and activity (Deisseroth et al., 2004; Gould et al., 1997; Song et al., 2012; Stone et al., 2011; Tozuka et al., 2005). However, it remains to be examined whether regulation for determining the site of neuronal addition exists in the dentate gyrus.

Previous studies have shown activity-dependent mechanisms that may allow for local regulation of neuronal birth through direct interactions between neural stem cells and neurons. The extensive processes of neural stem cells/radial astrocytes are located inside the granule cell layer, thereby forming direct contacts with granule cells (Seri et al., 2004). A study suggested that through these cell-cell contacts, the activation of granule cells induces cell division of neural stem cells and facilitates their offspring to take neuronal lineage (Dong et al., 2019). Neural stem cells also send bushy processes to the inner part of molecular layer and ensheathe synapses from mossy cells to granule cells (Moss et al., 2016). Activation of mossy cell axons was shown

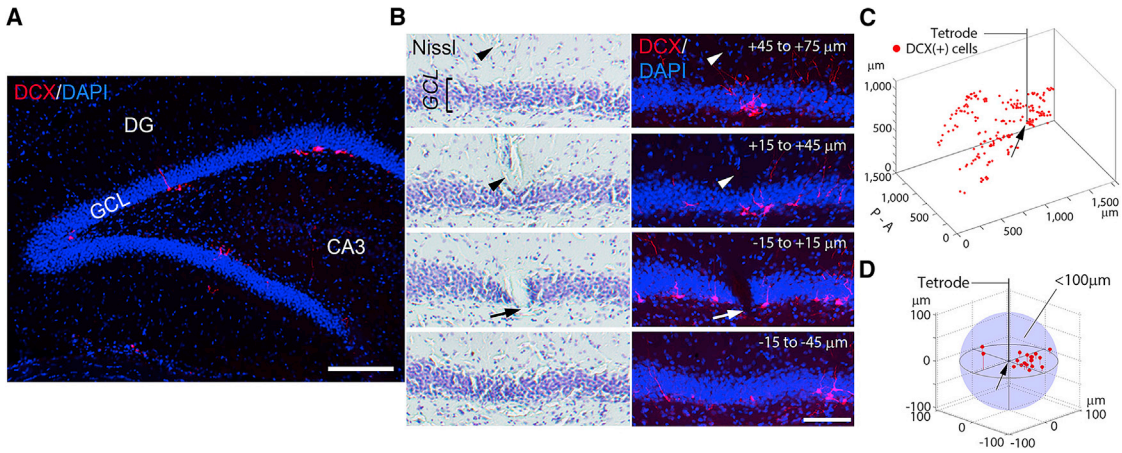

Figure 1. 3D reconstruction of the distribution of DCX(+) cells and recording sites

(A) Image showing the sparse distribution of DCX(+) cells in the dentate gyrus of a middle-aged rat. Scale bar, 200 μm.

(B) Determination of a recording site and distribution of DCX(+) cells nearby. (Left) Images from cresyl-violet-stained serial sections. The tetrode traces (arrowheads) were tracked through the serial sections. The ventral end of the trace (arrow) was determined as a recording site. GCL, granule cell layer. (Right) Fluorescence images of the same sections show the distribution of DCX(+) cells around the recording site. Scale bar, 100 μm. The number at the top-right corner of each image indicates the distance from the center of the section containing the recording site.

(C) 3D distribution of DCX(+) cells. Red dots, locations of DCX(+) cells; arrow, recording site shown in (B); A-P, anterior to posterior.

(D) Magnified view of the area around the recording site shown in (B). Blue sphere < 100 μm of the recording site (arrow).

See also Data S1.

to modulate neural stem cell activation (Yeh et al., 2018). In addition, the activation of parvalbumin-positive (PV(+)) interneurons was shown to inhibit neural stem cell activation (Song et al., 2012). These activity-dependent regulations through cell-cell contacts are suited as a mechanism to couple local neuronal activity to neuronal birth nearby and support the existence of such local regulation. However, another requirement for the existence of such local regulation is the existence of a positional relationship between neuronal activity and neurogenesis, which has not been described previously. Considering the role of the dentate gyrus in spatial processing (Gilbert et al., 1998; McNaughton et al., 1989; Treves et al., 2008), we monitored neuronal activity during spatial exploration and then examined anatomical relationships with neurogenesis.

RESULTS

Anatomical association between neurogenesis and place-cell activity in the dentate gyrus

We performed unit recording from the dentate gyrus during a food-foraging task in open-field environments. Rats went through food-foraging sessions for 2.5 weeks or longer before the final recording was performed at the age of 11–14 months. In middle-aged rats, the amount of neurogenesis is relatively low in the dentate gyrus (Kuhn et al., 1996) (Figure 1A; upper blade, 1.27 ± 0.65 × 10^3 cells/mm^3, and lower blade, 1.79 ± 0.91 × 10^3 cells/mm^3 of granule-cell-layer volume in mean ± SD). We detected single-unit activity that putatively originated from excitatory principal cells and inhibitory interneurons as previously described (Jung and McNaughton, 1993; Leutgeb et al., 2007; Nitz and McNaughton, 2004). We perfusion-fixed the rats 90 min after the final recording. All data presented in this part of study (Figures 1, 2, 3, 4, and 5) were acquired on the final recording days. In six rats, we found 43 recording sites located within or near the granule cell layer (Figure 1B).

To analyze the distribution of immature neurons, we acquired fluorescent images from serial sections immunostained against a marker for neuronal progenitors and immature neurons, doublecortin (DCX) (Figure 1B) (Brown et al., 2003). Through these images, we reconstructed a 3D distribution of DCX-positive (DCX(+)) cells and the recording sites (Figure 1C; Data S1A), from which we measured the distances from individual recording sites to DCX(+) cells (Figure 1D; Data S1B). From the 43 recording sites, we detected 24 putative principal cells, among which 19 were categorized as place cells (Figure S1; Data S2A). In addition, we found 38 putative interneurons. The number of isolated units per recording sites (1.74 ± 1.38 cells/recording site in mean ± SD) was similar to that in a previous study using similar recording conditions (Leutgeb et al., 2007). Placement of tetrodes did not appear to affect local neurogenesis, because the number of DCX(+) cells near recording sites (<100 μm) was not significantly different from the number of DCX(+) cells near randomly selected locations in the dentate gyrus (Figure S2A).

To examine the positional relationship between DCX(+) cells and active principal cells, we classified the 43 recording sites according to two factors: (1) whether recording sites had DCX(+) cells nearby (<100 μm) and (2) whether recording sites detected principal-cell activity. We found that 18 recording sites had DCX(+) cells nearby, whereas 25 did not; these are called DCX(+) and DCX-negative (DCX(−)) recording sites, respectively (Figures 2A and 2B; Data S1B). 17 recording sites detected principal-cell activity, whereas 26 did not (called principal-cell(+) and principal-cell(−) recording sites, respectively) (Figures 2A and 2B; Data S2A). Principal-cell(+) and principal-cell(−) recording sites

CellPress
OPEN ACCESS

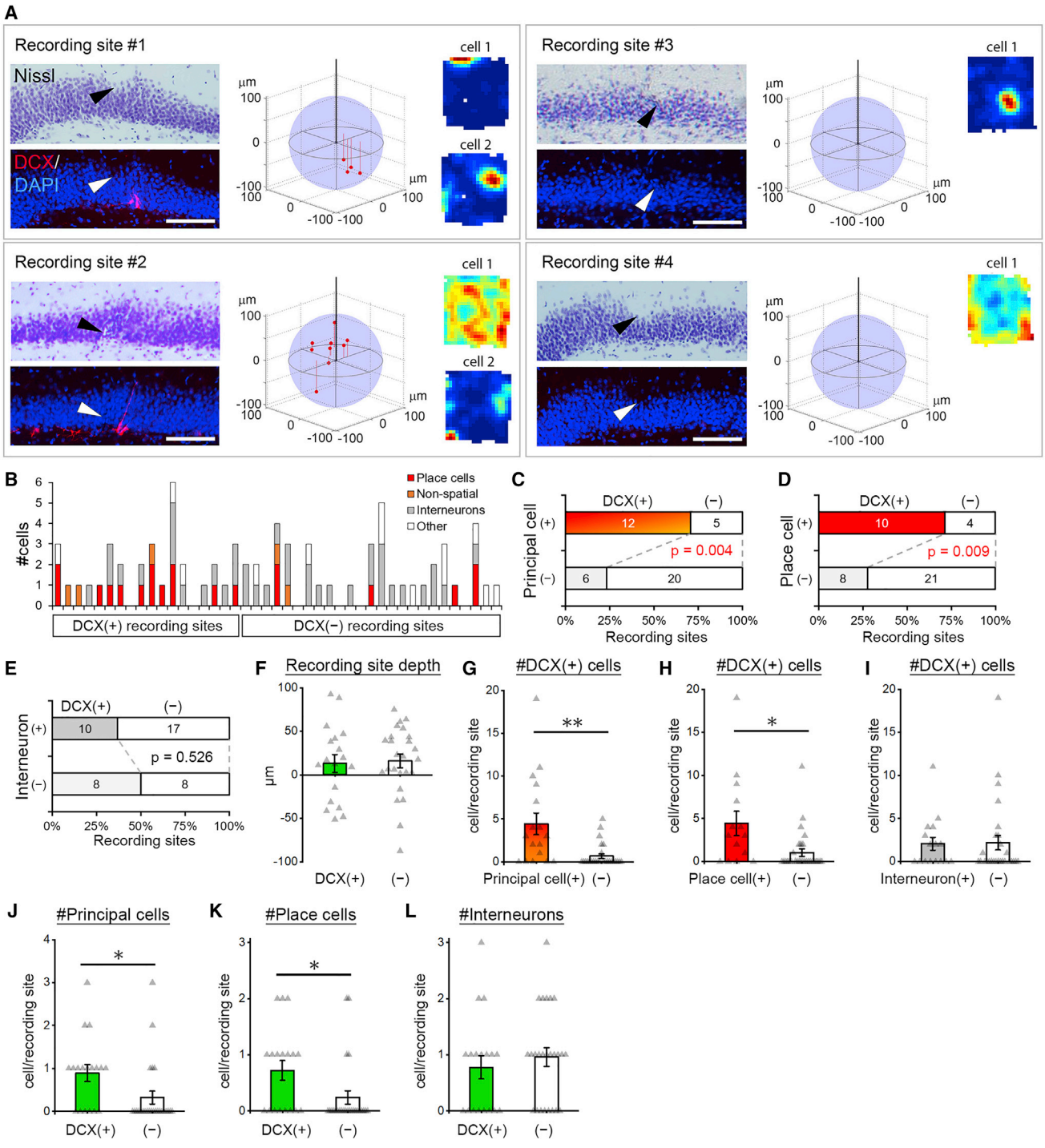

Figure 2. Anatomical association between place cells and DCX(+) cells

(A) Characterization of 4 example recording sites. (Left) Images from cresyl-violet-stained sections indicate the recording sites (black arrowheads). Fluorescence images from the same sections show the distribution of DCX(+) cells around the recording sites (white arrowheads). Scale bars, 100 µm. (Middle) 3D distribution of DCX(+) cells. (Right) Firing rate map of unit activity detected from the recording sites. See also Figure S1 and Data S2.

(B) Numbers of different cell types detected in individual recording sites. The 43 recording sites are sorted according to DCX(+) or DCX(−).

(C) Percentages of principal-cell(+) or principal-cell(−) recording sites that were DCX(+) or DCX(−). The numbers in the bar graphs are the numbers of recording sites. The p value is from Fisher's exact test.

(D) Same as (C) for place-cell(+) and place-cell(−) recording sites.

(E) Same as (C) for interneuron(+) and interneuron(−) recording sites.

(legend continued on next page)

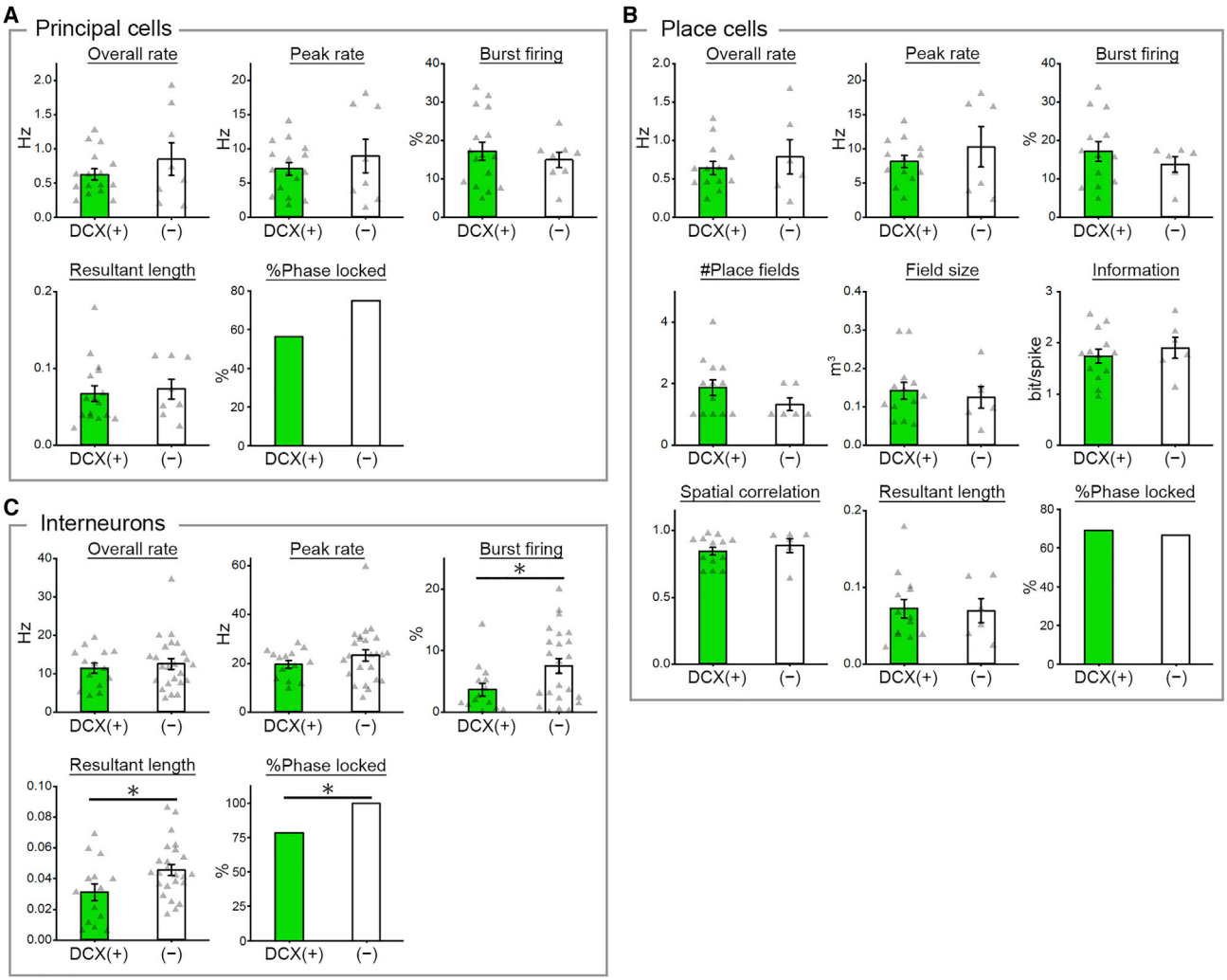

Figure 3. Firing properties of place cells and interneurons detected in DCX(+) and DCX(−) recording sites

(A) Firing properties of principal cells detected in DCX(+) and DCX(−) recording sites (n = 16 and 8, respectively). None of the properties are significantly different. $p > 0.3$ for all, Fisher's exact test for %Phase locked, independent-sample t tests for others.

(B) Firing properties of place cells detected in DCX(+) and DCX(−) recording sites (n = 13 and 6, respectively). None of the properties are significantly different. $p > 0.2$ for all, Fisher's exact test for %Phase locked, independent-sample t tests for others.

(C) Firing properties of interneurons detected in DCX(+) and DCX(−) recording sites (n = 14 and 24, respectively). Bursting tendency and resultant length are significantly lower in interneurons detected in DCX(+) recording sites ($p = 0.022$ and 0.032, respectively, independent-sample t tests). The proportion of interneurons significantly phase locked to theta oscillations is significantly lower in interneurons detected in DCX(+) recording sites ($p = 0.043$, Fisher's exact test). Overall and peak rates are not significantly different ($p = 0.598$ and 0.284, respectively, independent-sample t tests). Data (except %Phase locked) are represented as mean ± SEM with individual data points.

may or may not have detected interneurons or other cell types, but in this part of analysis, we focused on the presence/absence of active principal cells only. As shown in Figure 2C (also see Figure S2B), of the 17 principal-cell(+) recording sites, 12 were DCX(+) (70.6%), whereas the other 5 were DCX(−). In contrast, of the 26 principal-cell(−) recording sites, 6 were DCX(+) (23.1%), whereas 20 were DCX(−). Thus, the likelihood that recording sites were close to DCX(+) cells is different depending

(F) Depth of DCX(+) and DCX(−) recording sites. The border between the granule cell layer and the hilus is defined as 0. The distances in the directions to the granule cell layer and hilus are expressed as positive and negative values, respectively. $p = 0.812$, independent-sample t test. See Figures S2D and S4B.

(G–I) Number of DCX(+) cells within 100 μm of principal-cell(+) and principal-cell(−) recording sites (G, n = 17 and 26, respectively), place-cell(+) and place-cell(−) recording sites (H, n = 14 and 29, respectively), or interneuron(+) and interneuron(−) recording sites (I, n = 27 and 16, respectively). $p = 0.010$ (G), 0.038 (H), 0.922 (I), independent-sample t tests.

(J–L) Number of active principal cells (J), place cells (K), or interneurons (L) detected in DCX(+) and DCX(−) recording sites (n = 18 and 25, respectively). $p = 0.024$ (J and K), 0.495 (L), independent-sample t tests. Data in (F)–(L) are represented as mean ± SEM with individual data points. See also Figures S2 and S3.

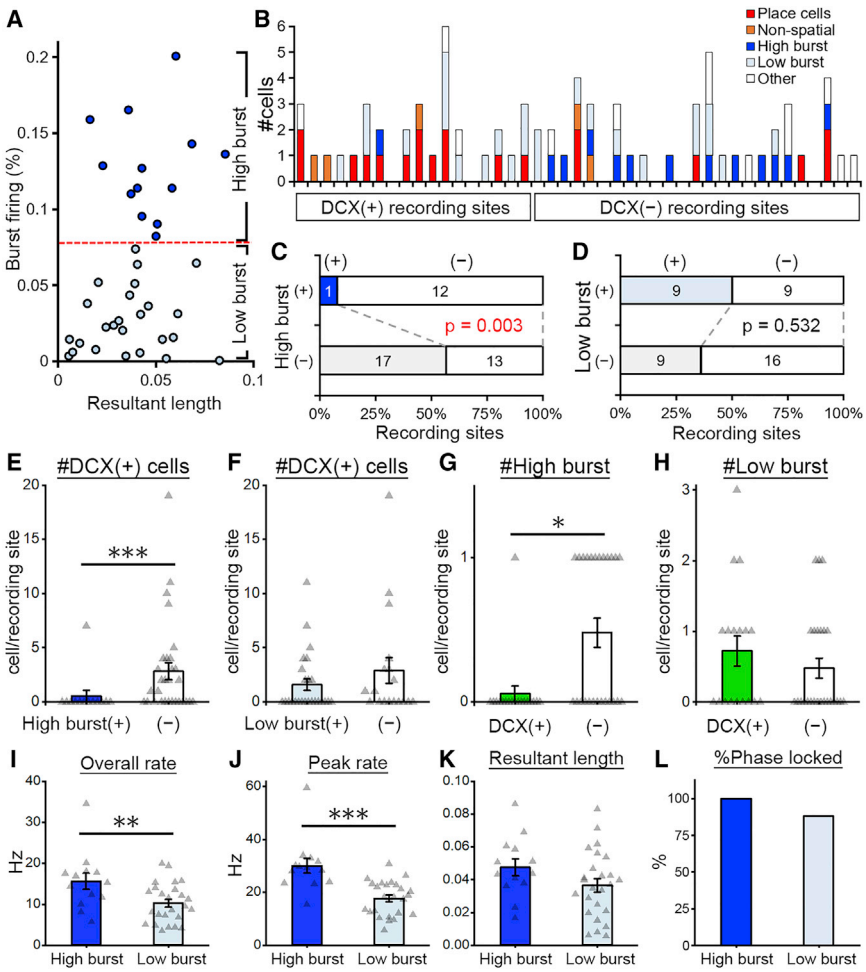

Figure 4. Anatomical dissociation between high-burst interneurons and DCX(+) cells

(A) Scatterplot showing bursting and resultant length of individual interneurons. Blue and light blue circles, high- and low-burst interneurons, respectively.

(B) Numbers of different cell types detected in individual recording sites.

(C) Percentages of high-burst interneuron(+) or interneuron(−) recording sites that were DCX(+) or DCX(−). The numbers in the bar graphs are the numbers of recording sites. The p value is from Fisher's exact test.

(D) Same as (C) for low-burst interneuron(+) and interneuron(−) recording sites.

(E and F) Number of DCX(+) cells within 100 μm of high-burst interneuron(+) and interneuron(−) recording sites (E, n = 13 and 30, respectively) or low-burst interneuron(+) and interneuron(−) recording sites (F, n = 18 and 25, respectively). p = 0.021 (E), 0.288 (F), independent-sample t tests.

(G and H) Number of high-burst (G) or low-burst (H) interneurons detected in DCX(+) and DCX(−) recording sites (n = 18 and 25, respectively). p = 0.0008 (G), 0.330 (H), independent-sample t tests.

(I–L) Firing properties of high- and low-burst interneurons (n = 13 and 25, respectively). Overall and peak rates are significantly higher in high-burst interneurons than low-burst interneurons. p = 0.0096 (I), p = 0.001 (J), independent-sample t tests. Resultant length and proportion of neurons significantly phase locked to theta oscillations are not significantly different. p = 0.114, independent-sample t test (K); p = 0.538, Fisher's exact test (L). Data in (E)–(K) are represented as mean ± SEM with individual data points. See also Figure S4.

on whether they detected principal-cell activity. This dependency between the two factors was statistically significant (Figure 2C), which suggests that DCX(+) cells and principal-cell activity are positionally associated with each other. We performed the same analysis for place cells and putative interneurons. As shown in Figure 2D, of the 14 place-cell(+) recording sites, 10 were DCX(+) (71.4%), whereas the other 4 were DCX(−). In contrast, of the 29 place-cell(−) recording sites, 8 were DCX(+) (27.6%), whereas 21 were DCX(−). The likelihood that recording sites were close to DCX(+) cells is significantly different depending on whether they detected place-cell activity (Figure 2D), suggesting a significant association. However, the same analysis did not find a significant relationship between DCX(+) cells and interneurons (Figure 2E). Because the 100-μm threshold for DCX(+) cells is somewhat arbitrary, we examined statistical significance with different thresholds and observed that the significant association of DCX(+) cells with principal-cell and place-cell activity was maintained at thresholds of 70–120 and 80–120 μm, respectively (Figure S2C). The association between DCX(+) cells and interneurons remained non-significant at the applied thresholds (Figure S2C). Distribution of DCX(+) and DCX(−) recording sites was similar in terms of depth relative to the border of the hilus and granule cell layer (Figures 2F, S2D, and S4B).

We examined the number of DCX(+) cells near the recording sites (<100 μm) and found significantly more DCX(+) cells around principal-cell(+) and place-cell(+) recording sites than around principal-cell(−) and place-cell(−) ones, respectively (Figures 2G and 2H), whereas no significant difference was observed between interneuron(+) and interneuron(−) recording sites (Figure 2I). In addition, we examined the number of active principal cells, place cells, or interneurons recorded in individual recording sites and found that higher numbers of active principal cells and place cells were detected in DCX(+) recording sites than in DCX(−) ones (Figures 2J and 2K), whereas the number of interneurons was similar between DCX(+) and DCX(−) recording sites (Figure 2L). These observations support the anatomical association of DCX(+) cells with principal cells and place cells.

Six of 43 recording sites did not detect isolated neuronal activity, which may result from the low quality of electrodes and could erroneously bias statistical analyses. To exclude this potential problem, we performed the analyses by removing these six recording sites (Figures S2E–S2M and S4C–S4H); the result was consistent with the original analyses.

We examined whether similar anatomical association can be observed between DCX(+) cells and excitatory neurons

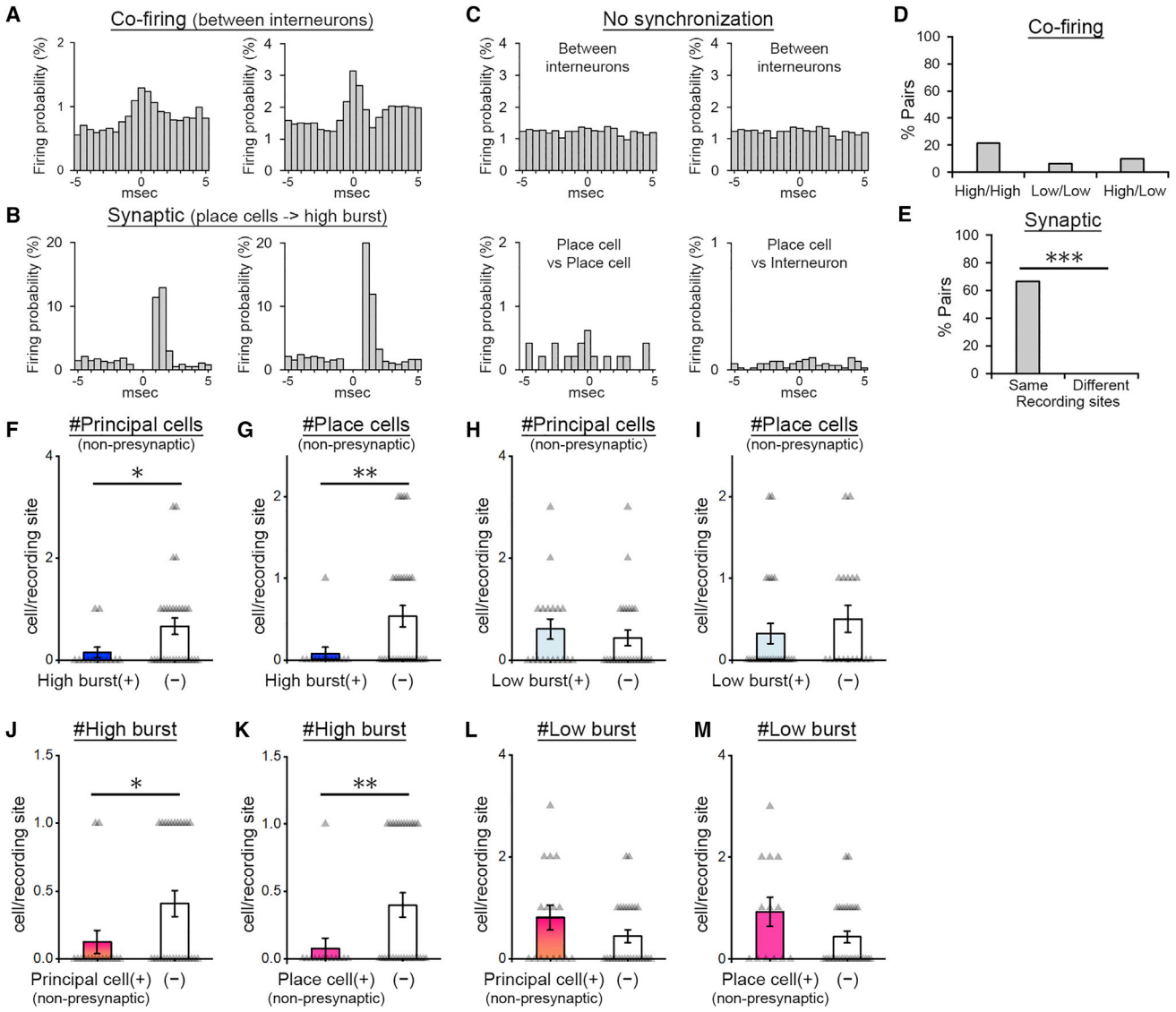

Figure 5. Putative excitatory synaptic connections from place cells to high-burst interneurons in the same recording site

(A–C) Firing cross-correlograms show the firing probability of a target neuron around the time of firing in a reference neuron (time 0). See also Table S1. (A) Two examples showing co-firing between interneurons. (B) Two cases showing putative excitatory synaptic connections from place cells to high-burst interneurons. (C) Four examples showing no synchronization.

(D) Percentage of interneuron pairs showing co-firing. Differences were not significant. p = 0.128 (high/high versus high/low), 0.354 (high/high versus low/low), 0.717 (high/low versus low/low), Fisher's exact test.

(E) Percentage of pairs of place cells and high-burst interneurons showing the excitatory synaptic connection. A significantly higher percentage of pairs detected in the same recording sites showed a synaptic connection compared with pairs detected in the different recording sites. p = 0.0038, Fisher's exact test.

(F–I) Number of non-presynaptic principal cells (F and H) and place cells (G and I) detected in high-burst(+) and high-burst(−) recording sites (F and G, n = 13 and 30, respectively) or in low-burst(+) and low-burst(−) recording sites (H and I, n = 18 and 25, respectively). p = 0.011 (F), p = 0.005 (G), 0.494 (H), 0.384 (I), independent-sample t tests.

(J–M) Number of high-burst (J and K) or low-burst (L and M) interneurons detected in non-presynaptic principal cell(+) or principal cell(−) recording sites (J and L, n = 16 and 27, respectively) or place cell(+) or place cell(−) recording sites (K and M, n = 13 and 30, respectively). p = 0.034 (J), 0.00998 (K), 0.193 (L), 0.133 (M), independent-sample t tests. Data in (F)–(M) are represented as mean ± SEM with individual data points.

expressing an immediate early gene, c-*fos*. However, we did not detect a significant anatomical relationship between DCX(+) cells and c-*fos*(+) cells (Figure S3). The observation reminded us of previous findings suggesting that the assumption of "c-*fos*(+) cells = place cells or active principal cells during the foraging sessions" is wrong. It is known that many silent principal cells during foraging sessions become active during resting periods before, between, and after the foraging sessions (Neunuebel and Knierim, 2012), and these neurons may express c-*fos*. It has been shown that in CA1, only one-fourth of place cells are

c-*fos*(+) and the remaining three-fourths are c-*fos*(−) (Tanaka et al., 2018). Therefore, many place cells do not express c-*fos*.

Anatomical dissociation between neurogenesis and high-burst interneurons

We compared firing properties of principal cells, place cells, and interneurons detected in DCX(+) and DCX(−) recording sites, including overall rate, peak rate, bursting tendency, place-field size, and parameters for theta phase locking. Principal cells and place cells recorded from DCX(+) and DCX(−) recording sites did not show a significant difference in the examined parameters (Figures 3A and 3B). In contrast, interneurons showed significant differences in two parameters (Figure 3C). First, interneurons detected in DCX(+) recording sites showed a lower tendency toward burst firing (a train of multiple firings with a <10 ms inter-spike interval) than did interneurons detected in DCX(−) recording sites (Figure 3C). Second, interneurons detected in DCX(+) recording sites less strongly phase locked to theta oscillations, as shown by lower values of the resultant length and proportion of significantly phase-locked cells, than did interneurons from DCX(−) recording sites (Figure 3C).

Because interneurons in the dentate gyrus consist of multiple subtypes that show different firing characteristics, including bursting tendency and theta phase locking, we reasoned that the significant differences detected earlier may occur because different types of interneurons are located between the area around DCX(+) and DCX(−) recording sites. Therefore, we classified interneurons using bursting tendency and resultant length for theta phase locking. We performed k-means clustering to separate 38 interneurons into 2 to 6 classes and evaluated the validity of classification by the silhouette method. The result indicated that classifying into 2 classes is most appropriate. By plotting the two classes of interneurons as in Figure 4A, we noted that the two groups can be divided by a threshold in bursting tendency even without considering resultant length. Therefore, we decided to call the two classes high-burst and low-burst interneurons (13 and 25 cells, respectively).

We examined the positional relationship of high- and low-burst interneurons with DCX(+) cells. 13 high-burst interneurons were detected in 13 recording sites, whereas none occurred in the other 30 recording sites (called high-burst(+) and high-burst(−) recording sites, respectively) (Figure 4B). 25 low-burst interneurons were detected in 18 recording sites, whereas none occurred in the other 25 recording sites (called low-burst(+) and low-burst(−) recording sites, respectively). Among the 13 high-burst(+) recording sites, only one had DCX(+) cells within 100 μm (7.7%), whereas 12 did not (Figure 4C). Among the 30 high-burst(−) recording sites, 17 had DCX(+) cells within 100 μm (56.7%), whereas 13 did not. A significantly lower proportion of high-burst(+) recording sites had DCX(+) cells nearby compared with high-burst(−) recording sites, suggesting high-burst interneurons are positionally dissociated from DCX(+) cells. Low-burst interneurons did not show such a relationship with DCX(+) cells (Figure 4D). The significant dissociation between DCX(+) cells and high-burst interneurons was maintained at thresholds of 80–130 μm, whereas the relationship between DCX(+) cells and low-burst interneurons remained non-significant at the applied thresholds (Figure S4A). A significantly lower number of DCX(+) cells were near high-burst(+) recording sites compared with high-burst(−) ones (Figure 4E), whereas the number was not significantly different between low-burst(+) and low-burst(−) recording sites (Figure 4F). Furthermore, a significantly lower number of high-burst interneurons were recorded in DCX(+) recording sites than in DCX(−) ones (Figure 4G), whereas the number of low-burst interneurons was not significantly different between DCX(+) and DCX(−) recording sites (Figure 4H). The results were similar after removing data from recording sites that did not detect active neurons (Figures S4C–S4H). These observations support anatomical dissociation between DCX(+) cells and high-burst interneurons.

Overall and peak rates are significantly higher in high-burst interneurons than in low-burst interneurons, whereas the tendency toward phase locking to theta oscillations is not significantly different (Figures 4I–4L).

Putative synaptic connection from place cells to high-burst interneurons in the same recording sites

To evaluate how the different neuronal types interact, we examined the temporal relationship of firing between simultaneously recorded neurons (Fujisawa et al., 2008; Senzai and Buzsáki, 2017). We used timings of individual spikes in one neuron (reference neuron) as a reference (time 0) and counted the number of spikes in another neuron (target neuron) in time bins around time 0. From this count, we calculated the probability of firing in the target neuron in each 0.5-ms bin (Figures 5A–5C). From 335 simultaneously recorded pairs (Table S1), we found two types of synchronized firing. First, firing probability is significantly increased symmetrically around time 0 (Figure 5A), which indicates that the two neurons are activated together (co-firing), possibly by a common input source. Second, the probability of target neuron firing is significantly increased shortly after time 0 (Figure 5B), which suggests the existence of excitatory synapses from the reference neuron to the target neuron.

Co-firing occurred only between interneurons, with a slightly (not significantly) higher proportion of pairs between high-burst interneurons (n = 14 pairs in total) than between low-burst interneurons (n = 51 pairs) or between high- and low-burst interneurons (n = 47 pairs) (Figure 5D). No pairs between principal/place cells or between principal/place cells and interneurons showed co-firing (Figure 5C). Putative excitatory synaptic connections were found only from place cells to high-burst interneurons (Figure 5B). 66.7% (2/3) of pairs of place cells and high-burst interneurons recorded from the same recording sites showed putative excitatory connections, whereas no pairs between place cells and high-burst interneurons from different recording sites did so (Figure 5E); the proportion in pairs from the same recording site is significantly higher than that in pairs from different recording sites. Thus, when a place cell is close to a high-burst interneuron, the place cell is likely presynaptic to the high-burst interneuron; such a synaptic connection is less likely to exist or is sparser if the neurons are located far from each other.

The numbers of active principal and place cells not presynaptic to high-burst interneurons were significantly lower in high-burst(+) recording sites than in high-burst(−) recording sites (Figures 5F and 5G). There was no significant difference in those

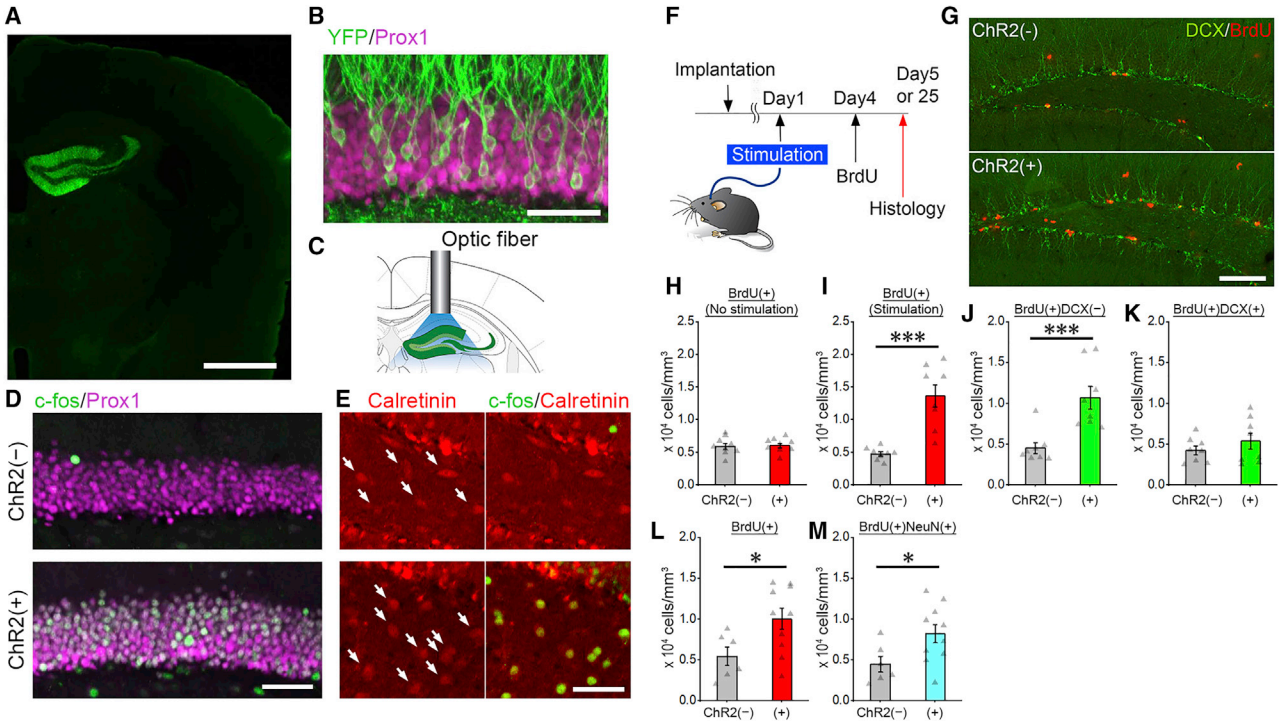

Figure 6. Brief optogenetic activation of excitatory neurons induces adult neurogenesis in the dentate gyrus

(A) Image showing ChR2-YFP expression in the dentate gyrus. Scale bar, 1 mm. See also Figure S5.

(B) ChR2-YFP is specifically expressed in granule cells. Scale bar, 50 μm.

(C) Schematic of an implanted optic fiber and light delivery through the fiber.

(D and E) Images showing c-*fos* expression in granule cells (D) and mossy cells (E) in ChR2(−) (top) and ChR2(+) (bottom) mice. Arrows, calretinin(+) cells (E, left). Light delivery induced c-*fos* expression in ChR2(+) mice. Scale bars, 50 μm.

(F) Experimental timeline.

(G–K) Histological analysis on day 5 in (F). (G) Images of the dentate gyrus of ChR2(+) and ChR2(−) mice after light stimulation. Scale bar, 100 μm. (H and I) BrdU(+) cell densities in ChR2(+) and ChR2(−) mice without (H) or with (I) light stimulation. (H) n = 9 mice for each, p = 0.855; (I) n = 8 mice for each, p = 0.001; independent-sample t tests. (J) BrdU(+)/DCX(−) cell densities. n = 8 mice for each, p = 0.002, independent-sample t test. (K) BrdU(+)/DCX(+) cell density. n = 8 mice for each, p = 0.335, independent-sample t test.

(L and M) BrdU(+) (L) and BrdU(+)/NeuN(+) double-positive (M) cell densities on day 25 in (F). n = 10 mice (ChR2(−)), 6 mice (ChR2(+)); p = 0.030 (L), 0.040 (M); independent-sample t tests. Data in (H)–(M) are represented as mean ± SEM with individual data points.

numbers between low-burst(+) and low-burst(−) recording sites (Figures 5H and 5I). The number of high-burst interneurons was significantly lower in recording sites with active principal cells or place cells, which are not presynaptic to high-burst interneurons, than in those without place cells, which are not presynaptic to high-burst interneurons (Figures 5J and 5K). In contrast, there is no significant difference for the numbers of low-burst interneurons (Figures 5L and 5M). Thus, active principal cells and place cells tend not to be close to high-burst interneurons unless they are presynaptic to the high-burst interneurons.

Brief optogenetic activation of granule cells induces neurogenesis in adult dentate gyrus

Previous studies suggested that principal cell activity induces local neuronal birth and/or PV(+) interneuron activity inhibits it (Dong et al., 2019; Song et al., 2012; Yeh et al., 2018). However, Only prolonged activation of neuronal types over several days has been evaluated; the effects of brief, discrete stimulation have never been examined. To extend the findings of previous studies, we examined whether brief activation is sufficient for the regulation of neuronal birth.

In the dentate gyrus, place-cell activity is generated by granule cells and mossy cells (GoodSmith et al., 2017; Senzai and Buzsáki, 2017). We used transgenic mice expressing channelrhodopsin-2 (H134R mutant) (Zhang et al., 2010) fused to yellow fluorescent protein (ChR2-YFP). In the dentate gyrus of these transgenic mice, ChR2-YFP was selectively expressed in ~10% of granule cells (Figures 6A, 6B, and S5). We delivered light pulses (473 nm, 1,800 × 10-ms pulses at 10 Hz) into the dentate gyrus of freely behaving mice (Figure 6C). This light delivery induced the expression of an immediate early gene, c-*fos*, in granule cells (Figure 6D) and their postsynaptic mossy cells (Figure 6E) in ChR2-YFP-expressing (ChR2(+)) mice, demonstrating optogenetic activation of both excitatory neuronal types.

To examine the impact of excitatory neuron activation on neurogenesis, we injected mice with 5-bromo-2′-deoxyuridine (BrdU) 3 days after light delivery and prepared brain sections 24 h after the BrdU injection (Figures 6F and 6G). Although without light

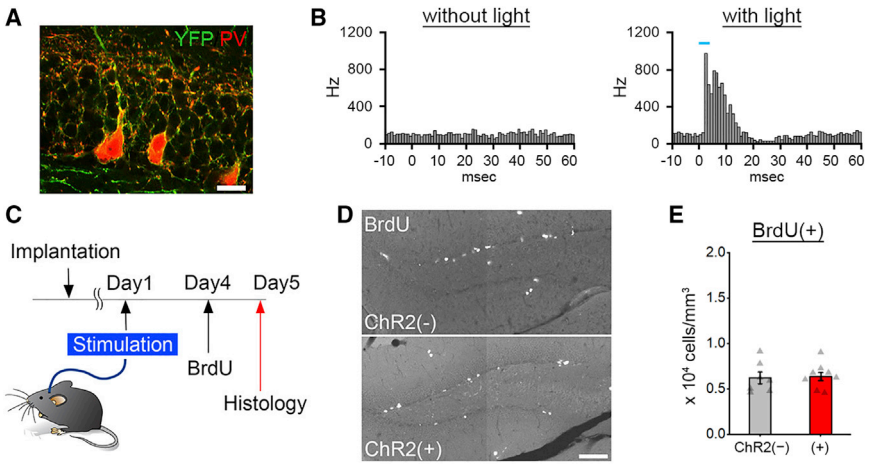

Figure 7. Brief optogenetic activation of PV(+) interneurons does not affect cell proliferation in the dentate gyrus

(A) Image showing specific ChR2-YFP expression in PV(+) neurons in the dentate gyrus of the PV-ChR2-YFP transgenic line. Green, YFP; red, PV. Scale bar, 20 μm.

(B) Multi-unit spike response to light stimulation in the dentate gyrus of PV-ChR2-YFP mice. Time 0 represents the onset of shutter opening without or with light (light blue bar).

(C) Experimental timeline.

(D) Images of BrdU(+) cells in the dentate gyrus of PV-ChR2(−) and PV-ChR2(+) mice. Scale bar, 100 μm.

(E) BrdU(+) cell density in the granule cell layer of PV-ChR2(+) mice (n = 9) and PV-ChR2(−) mice (n = 7) after light stimulation. p = 0.818, independent-sample t test. Data are represented as mean ± SEM with individual data points.

stimulation BrdU(+) cell densities were comparable between ChR2(+) and ChR2(−) mice (Figure 6H), BrdU(+) cell density was significantly higher in ChR2(+) mice than in ChR2(−) mice after light delivery (Figure 6I). This observation indicates that excitatory neuron activation induced cell proliferation. This was caused by an increase in BrdU(+)/DCX(−) cells, but not DCX(+)/BrdU(+) cells (Figures 6J and 6K). To examine the effect on neurogenesis, we quantified BrdU(+) cells and co-localization with a neuronal marker, NeuN, 21 days after BrdU injection. The densities of BrdU(+) and NeuN(+)/BrdU(+) cells were significantly higher in ChR2(+) mice than in ChR2(−) mice (Figures 6L and 6M). The proportion of NeuN(+) cells in the BrdU(+) cell population was comparable between ChR2(+) and ChR2(−) mice: ChR2(+) (n = 10), 53.4 ± 3.4 in %, and ChR2(−) (n = 6), 45.7 ± 6.1 in % (p = 0.597, independent-sample t test). These data indicate that excitatory neuron activation increases cell proliferation and neurogenesis.

We used a transgenic line expressing ChR2-YFP in PV(+) neurons (Figure 7A). Light delivery into the dentate gyrus increased multi-unit firing in the dentate gyrus of these mice (Figure 7B). We delivered light pulses in the same protocol used for excitatory neuron activation, injected BrdU 3 days after light delivery, and quantified BrdU(+) cell density 24 h after BrdU injection (Figure 7C). We did not find a significant difference in BrdU(+) cell density (Figures 7D and 7E). Thus, brief activation of PV(+) interneurons with this light delivery protocol did not affect cell proliferation.

DISCUSSION

Anatomical relationship between neuronal activity and neurogenesis in the adult dentate gyrus

Combining unit recording in freely moving rats with postfixed reconstruction of DCX(+) cell distribution, we determined whether individual recording sites were located close (<100 μm) to DCX(+) cells. The clusters of DCX(+) cells are sparsely scattered in the dentate gyrus of middle-aged rats, and their existence indicates the proximity to a neurogenic niche in which neurogenesis had occurred recently. Considering that single-unit isolation with a tetrode works efficiently when a neuron is located within ~50 μm of recording sites (larger mossy cells may be detected at a larger distance) (Henze et al., 2000), neurons detected in DCX(+) recording sites should be located at most within a few hundred micrometers from DCX(+) cells. We identified that the three electrophysiological features are positionally associated with a neurogenic niche: (1) the existence of principal/place cells, (2) the absence of high-burst interneurons, and (3) a lower tendency toward theta phase-locked firing in interneurons. Thus, neuronal activity and neurogenesis exhibit an anatomical relationship on such a small scale of a few hundred micrometers. Previous studies have indicated a local relationship at the level of brain structure (Bruel-Jungerman et al., 2006; Derrick et al., 2000; Dong et al., 2019; Song et al., 2012; Stone et al., 2011; Yeh et al., 2018), but not to such a high spatial resolution of a few hundred micrometers. These anatomical relationships indicate that a local neurogenic niche can be defined by these electrophysiological features and suggest that all or some of these electrophysiological features may be involved in a local regulation of structural and molecular characteristics of a microenvironment facilitating and/or inhibiting neurogenesis.

The distribution of DCX(+) cells that we analyzed was <3 h after the start of spatial exploration sessions (<1.5 h recording sessions + 1.5 h rest before perfusion). Although neuronal activity might have affected DCX(+) cell localization rapidly within 3 h, it is likely that neuronal activity during spatial exploration in the previous days had a major influence on the distribution of many DCX(+) cells we detected. The activity of place cells in the dentate gyrus is stable in a familiar environment over multiple days, in contrast to those in the CA1 and CA3 areas, which are highly unstable (Hainmueller and Bartos, 2018). In our experiments, the rats explored the same environments multiple times over many days. Therefore, a stable subset of neurons might have been activated over multiple days before the final recording sessions and have set up the positional relationship with DCX(+) cells.

Our data showed a statistically significant association between principal cells and DCX(+) cells, as well as between place cells and DCX(+) cells. This could be because DCX(+) cells show a positional association with principal cells in general (both place and non-spatial cells). Alternatively, only place cells, but not non-spatial principal cells, show this association; however, because

most principal cells in our dataset were place cells, we may still have detected significant association between principal cells and DCX(+) cells. Because the number of non-spatial cells is low, our data cannot dissociate the two possibilities.

Two types of excitatory neurons in the dentate gyrus, granule cells and mossy cells, display place-cell activity in the dentate gyrus (GoodSmith et al., 2017; Senzai and Buzsáki, 2017). Considering that we detected place cells from recording sites at different depths from the hilus to the border between the granule cell and the molecular layers (Figures 2F and S2D), it is likely that those active principal cells and place cells that we recorded include both granule cells and mossy cells. Granule cells send their axons down to the hilus and often form synapses onto nearby mossy cells. Senzai and Buzsáki (2017) have detected such functional connections between granule and mossy cells in unit recording with silicon probe electrodes. Connected pairs tended to be located, on average, ~60 μm apart. Therefore, when we detected place-cell activity exhibited by a granule cell in the granule cell layer, a postsynaptic mossy cell exhibiting place-cell activity would be located nearby, slightly below in the hilus. When we detected place-cell activity exhibited by a mossy cell, a presynaptic granule cell exhibiting place-cell activity would be located slightly above in the dentate gyrus. This proximity between a connected pair of a granule cell and a mossy cell may be why our excitatory neuron dataset contains a heterogeneous population of two cell types but still shows a clear positional relationship with DCX(+) cells. Alternatively, the positional association may have primarily come from mossy cells. Similar to previous studies using the same recording method, most place cells in our dataset had multiple place fields (Alme et al., 2010; Leutgeb et al., 2007). In addition, one of six rats underwent the final recording session in two environments, and all place cells detected in this rat were active in both environments (Data S2B). These are known features of mossy cells (GoodSmith et al., 2017; Senzai and Buzsáki, 2017). Therefore, our dataset of place cells (and principal cells) may have been dominated by mossy cells. Nonetheless, it is possible that the activity of two cell types is similarly linked to neurogenesis.

Although one may speculate that the cause of anatomical association between place cells and DCX(+) cells might be that DCX(+) cells generate place-cell activity, this is unlikely. First, in rats, DCX(+) cells are mostly <3 weeks old (Snyder et al., 2009a); although those immature neurons can generate action potentials in response to afferent stimulation, they hardly generate a burst of action potentials (Li et al., 2017). In contrast, place cells that we recorded from the dentate gyrus robustly fire bursts of action potentials. Second, juxtacellular recording from the dentate gyrus morphologically revealed that place cells are mossy cells and mature granule cells with highly elaborated dendrites (GoodSmith et al., 2017). Furthermore, we did not find DCX(+) cells in the vicinity of 4 of 14 recording sites that detected place-cell activity (Figure 2D), indicating that the existence of DCX(+) cells is not a requirement for the generation of place-cell activity nearby.

The neurochemical identity of high-burst interneurons is not known. However, the properties of high-burst interneurons we found are reminiscent of the previous findings on PV(+) interneurons in the hippocampus. First, PV(+) interneurons have a higher tendency toward burst firing than other interneurons in behaving mice (Royer et al., 2012). In addition, Gulyás et al. (2010) showed the same in brain slices. Second, the firing rate of PV(+) interneurons is higher than in other types of interneurons in behaving mice (Royer et al., 2012). We found that high-burst interneurons show a higher firing rate than low-burst interneurons (Figures 4I and 4J). Third, a large number of excitatory synaptic connections were found from excitatory neurons to PV(+) interneurons, whereas those to other types of interneurons were rarely found (Royer et al., 2012), which is reminiscent of our finding (Figures 5B and 5E).

Lateral inhibition circuits formed by excitatory and inhibitory neurons

Neuronal activity in the dentate gyrus is known to be highly sparse compared with other hippocampal and cortical regions; only a fraction of neurons are active, whereas most neurons are silent (Jung and McNaughton, 1993; Leutgeb et al., 2007; Neunuebel and Knierim, 2012). This is thought to be achieved by a winner-take-all kind of mechanism through lateral inhibition (de Almeida et al., 2009), in which a small number of active excitatory neurons stimulate inhibitory neurons, which in turn silence most other excitatory neurons. A study with brain slices showed that granule cells and PV(+) interneurons in the dentate gyrus are connected to form a lateral inhibition circuit (Espinoza et al., 2018). Furthermore, the probability and strength of these synaptic connections between granule cells and PV(+) interneurons rapidly reduces over the distance in the range of a few hundred micrometers (Espinoza et al., 2018; Strüber et al., 2015). Although such analysis for mossy cells and interneurons has not been done, it is known that mossy cells project excitatory outputs onto and receive inhibitory input from interneurons, including PV(+) interneurons (Freund and Buzsáki, 1996; Sun et al., 2017; Yeh et al., 2018), which is consistent with the idea that mossy cells are involved in lateral inhibition.

We found two relationships between place cells and high-burst interneurons that are consistent with the idea that they form a lateral inhibition circuit. First, although a place cell and a high-burst interneuron were rarely detected together in the same recording sites (Figure 4C), in most cases where this happened, the place cells fired 1–2 ms earlier than the high-burst interneurons (Figure 5B). This temporal relationship indicates that the place cells are presynaptic to the high-burst interneurons. Second, except these place cells that are presynaptic to high-burst interneurons, other place cells were less frequently found in high-burst(+) recording sites than in high-burst(−) recording sites (Figures 5G and 5K), suggesting that high-burst interneurons may silence nearby excitatory neurons, which are not presynaptic to the high-burst interneurons. These findings are consistent with the idea that granule cells, mossy cells, and interneurons that are located nearby at the range of ~100–200 μm form a local lateral inhibition circuit. Such a local excitatory-inhibitory neural circuit may underlie the local activity-dependent regulation of neurogenesis.

Regulation of adult neurogenesis by activity of excitatory and inhibitory neurons

We showed that the optogenetic activation of excitatory neurons increases cell proliferation (Figures 6I and 6J) and neurogenesis

(Figure 6M). A previous study showed that neural stem cell activation is inhibited and induced by moderate and strong, 4-day-long, chronic activation of axons from contralateral mossy cells, respectively (Yeh et al., 2018). Similar to the latter, another study found that 7-day, chronic, chemogenetic activation of granule cells resulted in the activation of neural stem cells and facilitated transition toward neuronal fates (Dong et al., 2019). Our findings are consistent with these studies and extend them two-fold. First, we demonstrated that brief stimulation (3 min × 3) within several hours is sufficient to induce cell proliferation, compared with chronic stimulation over 4 or 7 days used in the previous study. Second, we found that optogenetic activation of excitatory neurons not only induces cell proliferation but also increases neurogenesis, which has not been shown in the previous studies. We have discussed the remaining question of whether DCX(+) cells are anatomically associated with place cells specifically or principal cells generally. Related to this issue, optogenetic stimulation of excitatory neurons with an arbitrary temporal pattern increased neurogenesis, which would mean that place-cell firing pattern is not required to stimulate neurogenesis. However, it is possible that our light delivery protocol may have resulted in strong activation of excitatory neurons, which mimics some aspect of place-cell activity and is essential to facilitate local neurogenesis.

We optically stimulated PV(+) interneurons in the same one-day protocol used for excitatory neurons but did not observe changes in cell proliferation. Previous studies showed that the optogenetic activation of PV(+) interneurons over multiple days inhibited the activation of neural stem cells and cell proliferation (Song et al., 2012). Although brief activation is sufficient for the effect of excitatory neuron activation, chronic activation seems to be required for PV(+) interneurons to inhibit cell proliferation.

From these findings, we propose a local activity-dependent mechanism by which excitatory neuron activity induces the generation of new neurons nearby, presumably at the range of a few hundred micrometers or less. In addition, together with the previous finding that chronic activation of PV(+) interneurons inhibits the activation of neural stem cells, our finding of anatomical dissociation between neurogenesis and high-burst interneurons suggests that the activation of inhibitory neurons inhibits neurogenesis locally. Thus, activation of local excitatory circuits may recruit new neurons selectively nearby and at the same time induce the activation of surrounding inhibitory interneurons, which in turn limits the spatial range of the local recruitment of new neurons. This dual-activity-dependent process, possibly formed on a lateral inhibition circuit, may be a mechanism by which new neurons are selectively recruited into the microcircuit activated during a recent experience. The functional consequences of such selective neuronal recruitment may be the key to understanding the contribution of adult neurogenesis to adaptive brain functions at the microcircuit level.

STAR★METHODS

Detailed methods are provided in the online version of this paper and include the following:

SUPPLEMENTAL INFORMATION

Supplemental information can be found online at https://doi.org/10.1016/j.celrep.2021.109324.

ACKNOWLEDGMENTS

We thank Ms. Teruyo Tashiro and Ms. Chika Yoshii for their technical assistance. This work was supported by the Ministry of Education of Singapore (MOE2015-T2-2-035 and MOE2017-T3-1-002), NIMBELS (NIM/02/2016), National Medical Research Council of Singapore (NMRC/OFIRG/0046/2017), European Research Council (208132), Research Council of Norway (FRIBIO, 197184), James S. McDonnell Foundation (to A.T.), and Human Frontiers Science Programme (to M.U.).

AUTHOR CONTRIBUTIONS

M.U., S.B., and A.T. designed the experiments. M.U., S.B., L.F.C., and L.K.K. performed the experiments. All authors analyzed the data and wrote the manuscript.

DECLARATION OF INTERESTS

The authors declare no competing interests.

Received: January 2, 2016
Revised: May 23, 2021
Accepted: June 8, 2021
Published: July 6, 2021

REFERENCES

Aasebø, I.E., Blankvoort, S., and Tashiro, A. (2011). Critical maturational period of new neurons in adult dentate gyrus for their involvement in memory formation. Eur. J. Neurosci. *33*, 1094–1100.

Aasebø, I.E.J., Kasture, A.S., Passeggeri, M., and Tashiro, A. (2018). A behavioral task with more opportunities for memory acquisition promotes the survival of new neurons in the adult dentate gyrus. Sci. Rep. *8*, 7369.

Alme, C.B., Buzzetti, R.A., Marrone, D.F., Leutgeb, J.K., Chawla, M.K., Schaner, M.J., Bohanick, J.D., Khoboko, T., Leutgeb, S., Moser, E.I., et al. (2010). Hippocampal granule cells opt for early retirement. Hippocampus *20*, 1109–1123.

Bergami, M., Masserdotti, G., Temprana, S.G., Motori, E., Eriksson, T.M., Göbel, J., Yang, S.M., Conzelmann, K.K., Schinder, A.F., Götz, M., and Berninger, B. (2015). A critical period for experience-dependent remodeling of adult-born neuron connectivity. Neuron *85*, 710–717.

Biebl, M., Cooper, C.M., Winkler, J., and Kuhn, H.G. (2000). Analysis of neurogenesis and programmed cell death reveals a self-renewing capacity in the adult rat brain. Neurosci. Lett. *291*, 17–20.

Bragin, A., Jandó, G., Nádasdy, Z., Hetke, J., Wise, K., and Buzsáki, G. (1995a). Gamma (40–100 Hz) oscillation in the hippocampus of the behaving rat. J. Neurosci. *15*, 47–60.

Bragin, A., Jandó, G., Nádasdy, Z., van Landeghem, M., and Buzsáki, G. (1995b). Dentate EEG spikes and associated interneuronal population bursts in the hippocampal hilar region of the rat. J. Neurophysiol. *73*, 1691–1705.

Brown, J.P., Couillard-Després, S., Cooper-Kuhn, C.M., Winkler, J., Aigner, L., and Kuhn, H.G. (2003). Transient expression of doublecortin during adult neurogenesis. J. Comp. Neurol. *467*, 1–10.

Bruel-Jungerman, E., Davis, S., Rampon, C., and Laroche, S. (2006). Long-term potentiation enhances neurogenesis in the adult dentate gyrus. J. Neurosci. *26*, 5888–5893.

Buzsáki, G. (1986). Hippocampal sharp waves: their origin and significance. Brain Res. *398*, 242–252.

Christian, K.M., Song, H., and Ming, G.L. (2014). Functions and Dysfunctions of Adult Hippocampal Neurogenesis. Annu. Rev. Neurosci. *37*, 243–262.

de Almeida, L., Idiart, M., and Lisman, J.E. (2009). The input-output transformation of the hippocampal granule cells: from grid cells to place fields. J. Neurosci. *29*, 7504–7512.

Deisseroth, K., Singla, S., Toda, H., Monje, M., Palmer, T.D., and Malenka, R.C. (2004). Excitation-neurogenesis coupling in adult neural stem/progenitor cells. Neuron *42*, 535–552.

Deng, W., Aimone, J.B., and Gage, F.H. (2010). New neurons and new memories: how does adult hippocampal neurogenesis affect learning and memory? Nat. Rev. Neurosci. *11*, 339–350.

Derrick, B.E., York, A.D., and Martinez, J.L., Jr. (2000). Increased granule cell neurogenesis in the adult dentate gyrus following mossy fiber stimulation sufficient to induce long-term potentiation. Brain Res. *857*, 300–307.

Döbrössy, M.D., Drapeau, E., Aurousseau, C., Le Moal, M., Piazza, P.V., and Abrous, D.N. (2003). Differential effects of learning on neurogenesis: learning increases or decreases the number of newly born cells depending on their birth date. Mol. Psychiatry *8*, 974–982.

Dong, J., Pan, Y.B., Wu, X.R., He, L.N., Liu, X.D., Feng, D.F., Xu, T.L., Sun, S., and Xu, N.J. (2019). A neuronal molecular switch through cell-cell contact that regulates quiescent neural stem cells. Sci. Adv. *5*, eaav4416.

Espinoza, C., Guzman, S.J., Zhang, X., and Jonas, P. (2018). Parvalbumin^{+} interneurons obey unique connectivity rules and establish a powerful lateral-inhibition microcircuit in dentate gyrus. Nat. Commun. *9*, 4605.

Freund, T.F., and Buzsáki, G. (1996). Interneurons of the hippocampus. Hippocampus *6*, 347–470.

Fujisawa, S., Amarasingham, A., Harrison, M.T., and Buzsáki, G. (2008). Behavior-dependent short-term assembly dynamics in the medial prefrontal cortex. Nat. Neurosci. *11*, 823–833.

Ge, S., Goh, E.L., Sailor, K.A., Kitabatake, Y., Ming, G.L., and Song, H. (2006). GABA regulates synaptic integration of newly generated neurons in the adult brain. Nature *439*, 589–593.

Gilbert, P.E., Kesner, R.P., and DeCoteau, W.E. (1998). Memory for spatial location: role of the hippocampus in mediating spatial pattern separation. J. Neurosci. *18*, 804–810.

GoodSmith, D., Chen, X., Wang, C., Kim, S.H., Song, H., Burgalossi, A., Christian, K.M., and Knierim, J.J. (2017). Spatial Representations of Granule Cells and Mossy Cells of the Dentate Gyrus. Neuron *93*, 677–690.e5.

Gould, E., McEwen, B.S., Tanapat, P., Galea, L.A., and Fuchs, E. (1997). Neurogenesis in the dentate gyrus of the adult tree shrew is regulated by psychosocial stress and NMDA receptor activation. J. Neurosci. *17*, 2492–2498.

Gould, E., Beylin, A., Tanapat, P., Reeves, A., and Shors, T.J. (1999). Learning enhances adult neurogenesis in the hippocampal formation. Nat. Neurosci. *2*, 260–265.

Gulyás, A.I., Szabó, G.G., Ulbert, I., Holderith, N., Monyer, H., Erdélyi, F., Szabó, G., Freund, T.F., and Hájos, N. (2010). Parvalbumin-containing fast-spiking basket cells generate the field potential oscillations induced by cholinergic receptor activation in the hippocampus. J. Neurosci. *30*, 15134–15145.

Hainmueller, T., and Bartos, M. (2018). Parallel emergence of stable and dynamic memory engrams in the hippocampus. Nature *558*, 292–296.

Henze, D.A., Borhegyi, Z., Csicsvari, J., Mamiya, A., Harris, K.D., and Buzsáki, G. (2000). Intracellular features predicted by extracellular recordings in the hippocampus in vivo. J. Neurophysiol. *84*, 390–400.

Jung, M.W., and McNaughton, B.L. (1993). Spatial selectivity of unit activity in the hippocampal granular layer. Hippocampus *3*, 165–182.

Jung, M.W., Wiener, S.I., and McNaughton, B.L. (1994). Comparison of spatial firing characteristics of units in dorsal and ventral hippocampus of the rat. J. Neurosci. *14*, 7347–7356.

Kempermann, G. (2012). New neurons for 'survival of the fittest'. Nat. Rev. Neurosci. *13*, 727–736.

Kempermann, G., Kuhn, H.G., and Gage, F.H. (1997). More hippocampal neurons in adult mice living in an enriched environment. Nature *386*, 493–495.

Kuhn, H.G., Dickinson-Anson, H., and Gage, F.H. (1996). Neurogenesis in the dentate gyrus of the adult rat: age-related decrease of neuronal progenitor proliferation. J. Neurosci. *16*, 2027–2033.

Leutgeb, S., Leutgeb, J.K., Treves, A., Moser, M.B., and Moser, E.I. (2004). Distinct ensemble codes in hippocampal areas CA3 and CA1. Science *305*, 1295–1298.

Leutgeb, J.K., Leutgeb, S., Moser, M.B., and Moser, E.I. (2007). Pattern separation in the dentate gyrus and CA3 of the hippocampus. Science *315*, 961–966.

Li, L., Sultan, S., Heigele, S., Schmidt-Salzmann, C., Toni, N., and Bischofberger, J. (2017). Silent synapses generate sparse and orthogonal action potential firing in adult-born hippocampal granule cells. eLife *6*, e23612.

McNaughton, B.L., Barnes, C.A., Meltzer, J., and Sutherland, R.J. (1989). Hippocampal granule cells are necessary for normal spatial learning but not for spatially-selective pyramidal cell discharge. Exp. Brain Res. *76*, 485–496.

Moreno-Jiménez, E.P., Flor-García, M., Terreros-Roncal, J., Rábano, A., Cafini, F., Pallas-Bazarra, N., Ávila, J., and Llorens-Martín, M. (2019). Adult hippocampal neurogenesis is abundant in neurologically healthy subjects and drops sharply in patients with Alzheimer's disease. Nat. Med. *25*, 554–560.

Moss, J., Gebara, E., Bushong, E.A., Sánchez-Pascual, I., O'Laoi, R., El M'Ghari, I., Kocher-Braissant, J., Ellisman, M.H., and Toni, N. (2016). Fine processes of Nestin-GFP-positive radial glia-like stem cells in the adult dentate gyrus ensheathe local synapses and vasculature. Proc. Natl. Acad. Sci. USA *113*, E2536–E2545.

Muller, R.U., Kubie, J.L., and Ranck, J.B., Jr. (1987). Spatial firing patterns of hippocampal complex-spike cells in a fixed environment. J. Neurosci. *7*, 1935–1950.

Neunuebel, J.P., and Knierim, J.J. (2012). Spatial firing correlates of physiologically distinct cell types of the rat dentate gyrus. J. Neurosci. *32*, 3848–3858.

Nitz, D., and McNaughton, B. (2004). Differential modulation of CA1 and dentate gyrus interneurons during exploration of novel environments. J. Neurophysiol. *91*, 863–872.

Royer, S., Zemelman, B.V., Losonczy, A., Kim, J., Chance, F., Magee, J.C., and Buzsáki, G. (2012). Control of timing, rate and bursts of hippocampal place cells by dendritic and somatic inhibition. Nat. Neurosci. *15*, 769–775.

Senzai, Y., and Buzsáki, G. (2017). Physiological Properties and Behavioral Correlates of Hippocampal Granule Cells and Mossy Cells. Neuron *93*, 691–704.e5.

Seri, B., García-Verdugo, J.M., Collado-Morente, L., McEwen, B.S., and Alvarez-Buylla, A. (2004). Cell types, lineage, and architecture of the germinal zone in the adult dentate gyrus. J. Comp. Neurol. *478*, 359–378.

Skaggs, W.E., McNaughton, B.L., Gothard, K.M., and Markus, E.J. (1993). An Information-Theoretic Approach to Deciphering the Hippocampal Code. Adv. Neural Inf. Process. Syst. *5*, 1030–1037.

Snyder, J.S., Choe, J.S., Clifford, M.A., Jeurling, S.I., Hurley, P., Brown, A., Kamhi, J.F., and Cameron, H.A. (2009a). Adult-born hippocampal neurons are more numerous, faster maturing, and more involved in behavior in rats than in mice. J. Neurosci. *29*, 14484–14495.

Snyder, J.S., Radik, R., Wojtowicz, J.M., and Cameron, H.A. (2009b). Anatomical gradients of adult neurogenesis and activity: young neurons in the ventral dentate gyrus are activated by water maze training. Hippocampus *19*, 360–370.

Song, J., Zhong, C., Bonaguidi, M.A., Sun, G.J., Hsu, D., Gu, Y., Meletis, K., Huang, Z.J., Ge, S., Enikolopov, G., et al. (2012). Neuronal circuitry mechanism regulating adult quiescent neural stem-cell fate decision. Nature *489*, 150–154.

Sorrells, S.F., Paredes, M.F., Cebrian-Silla, A., Sandoval, K., Qi, D., Kelley, K.W., James, D., Mayer, S., Chang, J., Auguste, K.I., et al. (2018). Human hippocampal neurogenesis drops sharply in children to undetectable levels in adults. Nature *555*, 377–381.

Stone, S.S., Teixeira, C.M., Devito, L.M., Zaslavsky, K., Josselyn, S.A., Lozano, A.M., and Frankland, P.W. (2011). Stimulation of entorhinal cortex promotes adult neurogenesis and facilitates spatial memory. J. Neurosci. *31*, 13469–13484.

Strüber, M., Jonas, P., and Bartos, M. (2015). Strength and duration of perisomatic GABAergic inhibition depend on distance between synaptically connected cells. Proc. Natl. Acad. Sci. USA *112*, 1220–1225.

Sun, Y., Grieco, S.F., Holmes, T.C., and Xu, X. (2017). Local and Long-Range Circuit Connections to Hilar Mossy Cells in the Dentate Gyrus. eNeuro *4*, ENEURO.0097-17.2017.

Tanaka, K.Z., He, H., Tomar, A., Niisato, K., Huang, A.J.Y., and McHugh, T.J. (2018). The hippocampal engram maps experience but not place. Science *361*, 392–397.

Tashiro, A., Sandler, V.M., Toni, N., Zhao, C., and Gage, F.H. (2006). NMDA-receptor-mediated, cell-specific integration of new neurons in adult dentate gyrus. Nature *442*, 929–933.

Tashiro, A., Makino, H., and Gage, F.H. (2007). Experience-specific functional modification of the dentate gyrus through adult neurogenesis: a critical period during an immature stage. J. Neurosci. *27*, 3252–3259.

Tozuka, Y., Fukuda, S., Namba, T., Seki, T., and Hisatsune, T. (2005). GABAergic excitation promotes neuronal differentiation in adult hippocampal progenitor cells. Neuron *47*, 803–815.

Treves, A., Tashiro, A., Witter, M.P., and Moser, E.I. (2008). What is the mammalian dentate gyrus good for? Neuroscience *154*, 1155–1172.

van Praag, H., Kempermann, G., and Gage, F.H. (1999). Running increases cell proliferation and neurogenesis in the adult mouse dentate gyrus. Nat. Neurosci. *2*, 266–270.

Vanderwolf, C.H. (1969). Hippocampal electrical activity and voluntary movement in the rat. Electroencephalogr. Clin. Neurophysiol. *26*, 407–418.

Yeh, C.Y., Asrican, B., Moss, J., Quintanilla, L.J., He, T., Mao, X., Cassé, F., Gebara, E., Bao, H., Lu, W., et al. (2018). Mossy Cells Control Adult Neural Stem Cell Quiescence and Maintenance through a Dynamic Balance between Direct and Indirect Pathways. Neuron *99*, 493–510.e4.

Zhang, F., Gradinaru, V., Adamantidis, A.R., Durand, R., Airan, R.D., de Lecea, L., and Deisseroth, K. (2010). Optogenetic interrogation of neural circuits: technology for probing mammalian brain structures. Nat. Protoc. *5*, 439–456.

Zhao, C., Teng, E.M., Summers, R.G., Jr., Ming, G.L., and Gage, F.H. (2006). Distinct morphological stages of dentate granule neuron maturation in the adult mouse hippocampus. J. Neurosci. *26*, 3–11.

STAR★METHODS

KEY RESOURCES TABLE

REAGENT or RESOURCE	SOURCE	IDENTIFIER
Antibodies		
goat anti-DCX antibody (c-18)	Santa Cruz Biotechnology	sc-8066
rabbit anti-c-fos antibody	Santa Cruz Biotechnology	sc-52
rat anti-BrdU antibody	AbD Serotec	PBT00309
rabbit anti-GFP antibody	Invitrogen	A11122
goat anti-prox1	R&D systems	AF2727
rat anti-GFP	Nacalai Tesque	04404-84
Cy3-conjugated anti-rat IgG antibody		712-165-150
AlexaFluor488-conjugated anti-rabbit IgG antibody	Jackson ImmunoResearch	711-485-152
AlexaFluor647-conjugated anti-goat IgG antibody	Jackson ImmunoResearch	705-495-147
Cy3-conjugated anti-rabbit IgG antibody	Jackson ImmunoResearch	711-505-152
AlexaFluor488-conjugated anti-rat IgG antibody	Jackson ImmunoResearch	712-485-153
DyLight 488-conjugated anti-rabbit IgG antibody	Jackson ImmunoResearch	711-485-152
Cy3-conjugated donkey anti-goat IgG	Jackson ImmunoResearch	705-165-003
Experimental models: Organisms/strains		
Tg(Pomc1-cre)16Lowl/J	Jackson laboratory	Stock#005965
B6;129S-Gt(ROSA)26Sor$^{tm32(CAG-COP4*H134R/EYFP)Hze}$/J	Jackson laboratory	Stock#012569
B6;129P2-Pvalb$^{tm1(cre)Arbr}$/J	Jackson laboratory	Stock#008069
Software and algorithms		
MATLAB	MathWorks	N/A
MClust	Dr. A David Redish lab http://redishlab.neuroscience.umn.edu/mclust/MClust.html	N/A

RESOURCE AVAILABILITY

Lead contact

Further information and requests for resources and reagents should be directed to and will be fulfilled by the Lead Contact, Ayumu Tashiro (atashiro@ntu.edu.sg).

Materials availability

This study did not generate new unique reagents.

Data and code availability

Data and codes used in this study will be shared by the lead contract upon request.

EXPERIMENTAL MODEL AND SUBJECT DETAILS

Rats

We used six male Long-Evans rats (ID# 14741, 14742, 14933, 14934, 15096, and 15247) bred in our local animal facility or purchased from Charles River (Germany). Experiments were initiated when rats were 8–13 months old, and final recording experiments were performed at 9–15 months old. Rats were housed in acryl cages under 12-h light/12-h dark cycle conditions. We used middle-aged rats, in which DCX(+) cell densities are relatively low; this allowed for targeting recording electrodes to areas with or without nearby DCX(+) cells. All experiments were conducted according to approval by the Norwegian Animal Research Authority.

Mice

For optogenetic experiments with ChR2 expression in granule cells, we crossed two transgenic lines obtained from Jackson laboratory: a pomc-cre driver line [Stock#005965, Tg(Pomc1-cre)16Lowl/J] and a Cre-dependent channelrhodopsin-2 H134R line

[Stock#012569, B6;129S-Gt(ROSA)26Sor$^{tm32(CAG-COP4*H134R/EYFP)Hze}$/J]. For optogenetic experiments with ChR2 expression in PV(+) neurons, we crossed two transgenic lines obtained from Jackson laboratory: a PV-cre driver line [Stock#008069, B6;129P2-Pvalb$^{tm1(cre)Arbr}$/J] and the same Cre-dependent channelrhodopsin-2 H134R line. The mice were housed in plexiglass cages under inverted 12-h light/12-h dark cycle conditions with free access to water and food. Mice of either sex were implanted between 6 and 10 weeks after birth and stimulated between 7 and 13 weeks after birth. All experiments were conducted with approval from the Norwegian Animal Research Authority and IACUC at Nanyang Technological University.

METHOD DETAILS

Preparation and implantation of microdrives for rats

For unit recording, we used custom-made tetrodes composed of polyimide-coated platinum (90%)-iridium (10%) wires (California Fine Wire Company). Fourteen tetrodes were mounted on a microdrive, which allows 14 tetrodes to be moved independently. Twelve tetrodes were used to acquire unit and local field potential signals, and two were used for reference signals. Tetrode impedances were decreased to 150–300 kΩ at 1 kHz by plating with platinum. Rats were anesthetized with 3% isoflurane supplied with 1,000 ml/min air flow. Thereafter, isoflurane concentration was lowered to 2%. Lidocaine was applied to the scalp before incision for additional local anesthesia. Using a stereotaxic frame (Model 1430, David Kopf instruments, USA), the microdrive was positioned over the skull so that the center of the 14-tetrode bundle was located 4.0 mm posterior and 2.4 mm to the right of the bregma. The microdrive was fixed to the skull using screws anchored on the skull (cheesehead at size M1.6*3 mm) and dental cement (Meliodent, Heraeus Kulzer, Hsnau, Germany). We recorded positions of the 14 tetrodes on the microdrive and the direction of the implanted microdrive relative to the antero-posterior axis of the skull. This information allowed us to know the anteroposterior and medio-lateral distribution of the14 tetrodes, which was used to locate recording sites in post-fixed brain sections (see below).

Unit recording in rats

Each channel of tetrodes was connected with a preamplifier, HS-54 (Neuralynx, USA), which provides 48 channels, with unity gain amplification, and is equipped with light emitting diodes (LEDs). The rat's position, represented by the LEDs, was tracked with a video camera located over open fields at a sampling rate of 50 Hz. The output cables from the pre-amplifier were connected to a Digital Lynx recording system (Neuralynx, USA) through a slip-ring commutator. Unit activity was recorded with a band-pass filter of 600–6,000 Hz at a sampling rate of 32,556 Hz. Local field potential signals were monitored with a band-pass filter of 1–475 Hz at a sampling rate of 2,034.75 Hz. Immediately after microdrive implantation, all 14 tetrodes were lowered to 960 μm from the brain surface. Two reference tetrodes were lowered until firing activity became scarce, which corresponded to the area between the deep cortical layer and the hippocampus. The other 12 tetrodes were gradually lowered each day in steps of 80 μm or less toward the CA1 region and then in steps of 40 μm or less toward the dentate gyrus. Recording sites were estimated by characteristic features in a local field potential, such as theta oscillation (Vanderwolf, 1969) and sharp-wave ripples(Buzsáki, 1986) in the CA1 region and large-amplitude gamma oscillations (Bragin et al., 1995a) and dentate spikes (Bragin et al., 1995b) in the dentate gyrus. When background unit activity was increased in the dentate gyrus, the tetrodes were moved down by < 10 μm to acquire well isolated units during the foraging sessions.

Food foraging task

Rats underwent a food foraging task in open fields in dimly-lit rooms for 15 min. The open fields were 1 m × 1 m square shapes surrounded with four black walls. A small white square sheet was put on one wall of the open fields. After recovery from surgery, the daily amount of food given in home cages was restricted. The food amount in home cages was decreased or increased depending on whether or not rats performed the food foraging task well. During foraging sessions, small pieces of food were scattered into the open fields to encourage exploration all over the open fields. For rats 14741, 14742, 15096, and 15247, all foraging sessions were performed in the same open field, and final recording sessions consisted of two foraging sessions with 5 min rest in between. For rats 14933 and 14934, foraging sessions were performed in two identical open fields located in two different rooms. Final recording sessions consisted of four consecutive sessions in one and two open fields for rats 14934 and 14933, respectively.

Histological procedures after unit recording with rats

Ninety minutes after final recording sessions, rats were deeply anesthetized by inhalation of isoflurane and an intraperitoneal injection of equithesin. Rats were intracardially perfused with a 0.1M phosphate buffer and then with 4% paraformaldehyde in a 0.1M phosphate buffer. Fixed brains were removed from the skull and post-fixed with the 4% paraformaldehyde solution for 1 day at 4°C. The coronal brain sections were obtained at a 30 μm thickness at −20°C using cryostat (Microm HM550, Thermo scientific). Individual serial sections covering from the most anterior to ~1 mm posterior portion of the hippocampus, which included all the recording sites, were collected in an anteroposterior sequential order into 96-well plates filled with cryoprotection solution and stored at −20°C until being used. After rinsing sections with Tris-buffered saline (TBS), the sections were incubated in blocking solution (0.15% Triton X-100 and 5% donkey serum in TBS) for 30 min and then with goat anti-DCX antibody (c-18, Santa Cruz Biotechnology) in the blocking solution for 2 days at 4°C. The sections were rinsed with TBS, incubated with Cy3-conjugated donkey anti-goat IgG (Jackson ImmunoResearch) in the blocking solution for 2 days at 4°C, washed with TBS, and then incubated with 1 μg/ml 4,6-diamidino-2-phenylindol-dihydrochloride (DAPI) (MERCK) in TBS. The sections were mounted on glass slides with coverslips in an anteroposterior sequence and observed

under an epifluorescence microscope (Axioscope A1, Zeiss). Fluorescent images visualizing DCX immunoreactivity and DAPI were taken from individual sections with a 20 × objective lens. A pseudocolor image was made from two grayscale images representing DCX immunoreactivity and DAPI fluorescence, taken in the same field of view. After coverslips were removed, cresyl violet staining was performed on the section. Sections were then mounted by an Eukitt mounting medium (Prolab/VWR) after dehydration. Transmitted-light images were taken from individual sections with 10 × and 20 × objective lenses.

Determination of recording sites

The final positions of individual recording sites were determined by visually tracking the trace of tetrodes through cresyl-violet-stained serial sections. Based on information from the anteroposterior and mediolateral distribution of 14 tetrodes, which we recorded at the time of implantation, we matched traces in the serial sections with the individual tetrodes. The ventral ends of traces were determined as final recording sites. When the traces were faint, we confirmed the existence of the traces with a fluorescence filter, which often shows clearer contrast around the traces. When we were not able to track a tetrode trace through the serial sections, corresponding data were not included in further analyses.

For quantitative analyses, we represented each recording site by the center of the ventral end of a tetrode trace. We drew two lines for each recording site: one line forming the longitudinal central axis of the tetrode trace and the other line forming the ventral surface of the tetrode trace. The point at which these two lines meet was defined as a coordinate for the recording site. The recording site depth was measured from the nearest point on the boundary between the granule cell layer and the hilus. When recording sites were located at the sides of the granule cell layer and hilus, their depths were defined with positive and negative numbers, respectively (e.g., +50 μm, −50 μm). When the depths were between −100 and +100 μm, the recording sites were included in the analysis. This was because the majority of DCX(+) cells are located around the border between the granule cell layer and the hilus (depth 0). Virtually no DCX(+) cells could be found within 100 μm if we included recording sites at a depth of ≤ -100 or $\geq +100$ μm.

Reconstruction of a three-dimensional distribution of DCX(+) cells and recording sites

We reconstructed a three-dimensional distribution of DCX(+) cells and recording sites. First, fluorescence images taken from 34–37 serial sections were aligned with each other using Adobe Photoshop (Adobe systems). The alignment was performed using landmarks such as the granule cell layer visualized by DAPI staining and blood vessels forming holes. Next, we opened each aligned pseudocolor image in ImageJ (National Institutes of Health, USA) and recorded the x- and y-coordinates (in μm) of DCX(+) cells at the center of all cell bodies. We reconstructed the distribution of DCX(+) cells located at the upper blade and hinge regions of the granule cell layer. DCX(+) cells at the lower blade were excluded from the measurement since all the recording sites were positioned near the upper blade and hinge regions. The z coordinates (in μm) of DCX(+) cells were assigned according to the section number from the most anterior sections [z = 30 × (N-1) μm for DCX(+) cells in section number N]. Next, we determined the positions of recording sites in the fluorescence images from the serial sections. We overlaid the images from cresyl violet-stained sections containing recording sites with the corresponding fluorescence images. Then we identified precise positions of recording sites in the fluorescent images and recorded x, y, z-coordinates of each recording site in the same way as for the DCX(+) cells. Using these x, y, z-coordinates, we reconstructed a three-dimensional distribution of DCX(+) cells and recording sites (Figures 1C, 1D, and 2A; Data S1). We calculated distances between them in three dimensional space. In Figures 1D and 2A and Data S1B, the recording site was plotted at (0, 0, 0), and the plot was rotated around the anteroposterior axis so that the border line between the granule cell layer and the hilus at the recording site was parallel to the other horizontal axis in the graph.

In Figure S2A, we semi-randomly selected three locations for each recording site under the following conditions, 1) in the same sections and blade (upper or lower) as the recording site, 2) at the same depth relative to the hilar border of the granule cell layer as the recording site and 3) distributed evenly (they are not closed to each other or to the recording site) over imaged area of the same blade as the recording site. In this way, each of 43 recording sites have three selected locations. In each iteration of random selection, we randomly selected one of the three locations for each recording site. Then we calculated the average number of DCX(+) cells within 100 μm over the 43 selected locations. We repeated this 1,000,000 times. We compared the average number of DCX(+) cells within 100 μm of real recording sites with the 1,000,000 average numbers to evaluate whether the number of DCX(+) cells near recording sites was different from other locations semi-randomly chosen in the vicinity of the granule cell layer.

Spike sorting and unit classification

We only used unit recording data from the final recording sessions; the rats were perfusion-fixed 90 min after completion of the final recording sessions. We performed offline spike sorting using MClust software (Dr. A. Redish). We manually sorted spikes into clusters according to distributions in plots two-dimensionally projected by combinations of parameters (waveform amplitude, energy, and peak-to-valley recorded in each channel of a tetrode). Spikes in a well-isolated cluster were assigned to a single unit. Active units with mean firing rates (total number of spikes divided by session duration) > 0.1 Hz were included in subsequent analyses. For this purpose, mean firing rate of each unit was calculated for each session, and a mean value over all sessions for each unit was used for this criterion. For rat 14933, which underwent foraging sessions in two open fields, a mean value for each unit was calculated for the two open fields separately, and a higher value was used for this criterion. Among 75 well-isolated active units, 38 showed mean a firing rate $\geq$ 3.5 Hz and were classified as putative interneurons (Figure S1; Data S2). Out of the remaining 37 units, 24 were classified as principal cells according to their occasional burst firing, which was revealed by the existence of a peak within

10 msec in the distribution of interspike intervals (Figure S1; Data S2). The remaining thirteen were classified as "others." Nineteen principal cells showed spatially modulated firing patterns (spatial information: > 0.8 bits/sec), which were stable between sessions (Pearson correlation coefficients of the spatial correlations: > 0.5). These units were classified as place cells. Spatial information for each principal cell was calculated for each session, and a mean value over all sessions for each principal cell was used for the criterion. For rat 14933, we calculated, for each principal cell, spatial information for an open field with a higher mean firing rate and used it for the criterion. A spatial correlation for each principal cell was calculated for all pairs of sessions performed in the same open fields, and an average value for each principal cell was used for the criterion. For rat 14933, we calculated, for each principal cell, a spatial correlation for an open field with a higher mean firing rate and used it for the criterion. The remaining five principal cells were classified as "non-spatial" cells (Figure S1; Data S2).

To characterize the spatial distribution of firing patterns for individual units, we calculated firing rate maps (Leutgeb et al., 2004). The paths of rats' movements were smoothed by a mean filter. The open field arena was divided into 5 cm × 5 cm bins. For each bin, firing rate was calculated as Gaussian-filter-smoothed spike numbers in the bin divided by Gaussian-filter-smoothed time spent in the bin as follows:

Gaussian-filter-smoothed spike numbers in the k-th bin (k = 1, 2, 3,…, L):

$$S_k = \sum_{i=1}^{M} g\left(\frac{sx_i - X_k}{h}, \frac{sy_i - Y_k}{h}\right)$$

Gaussian-filter-smoothed duration spent in the k-th bin:

$$T_k = \sum_{j=1}^{N-1}\left[(t_{j+1} - t_j)\cdot g\left(\frac{A_x(t_{j+1}) - X_k}{h}, \frac{A_y(t_{j+1}) - Y_k}{h}\right)\right]$$

Firing rate in the k-th bin:

$$R_k = S_k / T_k$$

where (X_k, Y_k) is the center of the k-th bin, M is the total number of spikes during a recording session, N is the total number of position/time samples during the recording session, (sx_i, sy_i) is rat's position where the i-th spike occurred, $(A_x(t_j), A_y(t_j))$ is rat's position at the time of j-th position sample t_j, h is the Gaussian smoothing factor (set to 5 cm), and $g(x,y)$ is a 2D Gaussian kernel as follows:

$$g(x,y) = \frac{1}{\sqrt{2\pi}\,\sigma} exp\left(-\frac{x^2+y^2}{2\sigma^2}\right), (\sigma = 1.0)$$

To quantify the spatial specificity of firing for each unit, spatial information per spike, I, was calculated based on the information theory as follows (Jung et al., 1994; Skaggs et al., 1993):

$$I = \sum_{k=1}^{L}\left[\frac{T_k}{T}\cdot\frac{R_k}{R} log2\frac{R_k}{R}\right]$$

where T is the total duration $\left(T = \sum_{k=1}^{L} T_k\right)$, and R is the overall mean firing rate $\left(R = \frac{1}{L}\sum_{k=1}^{L} R_k\right)$.

To quantify the stability of spatial firing patterns of individual units, we examined the spatial correlation of firing maps between sessions (Muller et al., 1987). A Pearson's correlation coefficient (r) was calculated for a pair of sessions as follows:

$$r = \frac{\sum_{i=1}^{L}\left(R_{1k} - \overline{R_{1k}}\right)\left(R_{2k} - \overline{R_{2k}}\right)}{\sqrt{\sum_{i=1}^{L}\left(R_{1k} - \overline{R_{1k}}\right)^2}\sqrt{\sum_{i=1}^{n}\left(R_{2k} - \overline{R_{2k}}\right)^2}}$$

where R_{1k} and R_{2k} are the firing rates in the k-th bin during session 1 and 2, respectively, and $\overline{R_{1k}}$ and $\overline{R_{2k}}$ are the mean rates over all bins during session 1 and 2.

Other firing properties

We used a train of spikes with < 10-msec inter-spike interval as the definition of a burst. The tendency of burst firing was calculated as the number of bursts (counting each train as one) divided by the sum of numbers of bursts and single spikes (separated from previous and subsequent spikes with ≥ 10-msec intervals). Place fields are defined as contiguous spatial bins with a total area of ≥ 200 cm^2 and a peak rate of ≥ 1 Hz that consisted of a bin with firing rate of ≥ 20% of the peak rate . When there is a spatial bin with ≥ 1 Hz outside the first place field and the highest rate bins are not directly adjacent to the first place field, the second place field was defined in the same way as the first one. The same procedure was performed to define additional place fields. For theta phase lock analysis, local field potential signals were bandpass filtered at 6-10 Hz. Phases in theta oscillations were obtained by the Hilbert transformation

of the filtered local field potential signal. A phase at the closest timestamp to every spike timestamp was assigned to the spike. The mean resultant vector r was calculated as:

$$r = \sum_j e^{i\theta_j} / \mathrm{N}$$

where j denotes j-th spike and N is the total number of spikes. Resultant length, the strength of phase locking, was obtained as $|r|$. Every recorded spike in each session was assigned a spike phase θj, where j denotes the j-th spike.

Temporal relationship of firing between simultaneously recorded neurons

To evaluate how the different neuronal types interact in the circuit, we examined the temporal relationship of firing between simultaneously recorded neurons. We used timings of individual spikes in one neuron (reference neuron) as a reference (time 0) and counted the number of spikes in another neuron (target neuron) in time bins around time 0. From this count, we calculated the probability of firing in the target neuron in each 0.5-msec bin within ± 5.25 msec of firing in the reference neuron, by dividing the number of target neuron firing in each bin by the number of reference neuron firing. To identify statistically significant synchronized firing between neurons, we randomized the individual timing of target neuron firing relative to reference neuron firing by shifting the timings by random numbers between - 5 to +5 msec. Then we calculated the probability in each 0.5-msec bin and got the maximum probability value among all bins. For each cell pair, we repeated the data randomization 1,000,000 times. When the firing probabilities in two consecutive bins of real data were higher than 99.9999% of all maximum probability values from the randomized data, we judged that the cell pair shows significant synchronized firing. In its default setting, the Digital Lynx recording system put 750-μsec delay after detecting one neuronal firing until detecting a next firing in the same tetrode. Therefore, −0.75- to +0.75-msec bins (three 0.5-msec bins around zero) are always empty for cell pairs recorded from the same tetrodes. Considering this property, we randomized data for cell pairs from the same tetrodes in a modified way. When a randomized shift moves a timing of firing from < −0.75 to > −0.75, we added +1.5 msec (e.g., shifting −2 msec to +0.9 instead of −2 to −0.6, shifting −3 msec to +3.5 instead of −3 to +2). When a randomized shift moves at a timing of firing from > +0.75 to < +0.75, we subtracted 1.5 msec (e.g., shifting +1 msec to −2.5 instead of +1 to −1, shifting +2 msec to −1.6 instead of +2 to −0.1,). In this way, the data randomization keeps the three 0.5-msec bins zero while shifting the timings evenly to the other time bins.

Implantation of optic fiber connectors

We prepared LC simplex connectors (86024-5500, Thorlabs) equipped with optic fiber cable (core diameter: 105 μm, cat# AFS105/125Y, Thorlabs). The mice were anesthetized with isoflurane (induction with 3%, upkeep with 1%, airflow of 1,200 ml/min). After applying local anesthetic Marcain (40 μl, 0.25 mg/ml, SC) and analgesic Temgesic (0.03 mg/ml, 100 μl/mouse SC), we fixed the head in a stereotaxic frame (model 962, David Kopf instruments, USA). The skull was exposed with a single incision of the scalp, and then 6 holes were drilled into the skull for fixing screws and a seventh hole for optic fiber insertion. The hole for the fiber was drilled at a coordinate of 1.8 posterior and 1.2 mm lateral to the bregma in the right hemisphere. The tip of the fiber was lowered 1.6 mm ventrally from the skull surface. The optic fiber connector was fixed using dental cement (Meliodent, Heraeus Kulzer, Germany).

Light stimulation

After at least 3 days of recovery period from the implantation surgery, we applied light stimulation into the brain of implanted mice through the optic fiber. The stimulation protocol was 1,800 × 10 ms pulses at 10 Hz, which took 3 min. Light stimulations were performed once for immediate early gene expression analyses and repeated three times at 9, 13, and 17:00 h for 5-bromo-2′-deoxyuridine (BrdU) analyses.

Immunohistochemistry for optogenetic stimulation experiments

To label proliferating cells, we intraperitoneally injected a dose of BrdU (100 μg/g bodyweight, 10 mg/ml in 0.9%saline). We intracardially perfused the mice with 0.9% saline and, subsequently, 4% paraformaldehyde in a 0.1M phosphate buffer. We removed the brain from the skull and post-fixed it in 4% paraformaldehyde in a 0.1M phosphate buffer for 24 h at 4°C and incubated in 30% sucrose in a 0.1M phosphate buffer at 4°C for 1–7 days. We then sectioned the brain at 40 μm thickness using a freezing microtome at -36°C. The sections were kept in cryoprotection solution at −20°C. Before immunostaining was performed, the sections were rinsed in TBS three times for 10 min each. For BrdU immunostaining, the sections were first incubated in 50% deionized formamide (VWR international, 442543A) in 2 × saline-sodium citrate buffer (SSC) at 65°C for 2 h. The sections were rinsed in 2 × SSC for 15 min and then incubated with 2M HCl at 37°C for 30 min. Subsequently, the sections were rinsed for 10 min in a 0.1M borate buffer and 6 times for 15 min each in TBS. Thereafter, both BrdU and non-BrdU stained sections were treated in the same way as below. The sections were blocked by 60-min incubation with a blocking solution (3% donkey serum [sigma D9663], 0.25% Triton-X [sigma, T9284] in TBS) and incubated with primary antibodies in the blocking solution for 2 days. Primary antibodies used were: rat anti-BrdU (AbD Serotec, PBT00309, 1:500), rabbit anti-GFP (Invitrogen, A11122, 1:500), goat anti-DCX (Santa Cruz technology, sc-8066, 1:500), goat anti-prox1 (R&D systems, AF2727, 1:500), rabbit anti-c-Fos (Santa Cruz Biotechnology, sc-52, 1:500), and rat anti-GFP (Nacalai Tesque, 04404-84, 1:500). The sections were rinsed twice with TBS for 15 min and additionally with the blocking solution for 15 min, and then

incubated with secondary antibody (1:250 dilution) in the blocking solution for 4–6 h. The secondary antibodies used were raised in donkeys and purchased from Jackson ImmunoResearch Laboratories: Cy3-conjugated anti-rat IgG (712-165-150), AlexaFluor488-conjugated anti-rabbit IgG (711-485-152), AlexaFluor647-conjugated anti-goat IgG (705-495-147), Cy3-conjugated anti-rabbit IgG (711-505-152), and AlexaFluor488-conjugated anti-rat IgG (712-485-153). After incubation with 0.8 μg/ml DAPI in TBS for 10 min, the sections were rinsed three times with TBS (10 min each), mounted on glass slides, and covered with anti-fading mounting media and a coverslip.

Analyses of immunopositive cell densities for optogenetic stimulation experiments

We counted immunopositive cells in the granule cell layer and subgranular zone of the dentate gyrus in the sections covering the anteroposterior axis of the dentate gyrus (6–8 sections/mouse). The granule cell layer volume was calculated by multiplying section thickness (40 μm) by their area measured using ImageJ software (National Institute of Health, USA).

Multi-unit recording in mice

Neural activity was recorded by connecting the Digital Lynx recording system (Neuralynx, USA) through two head-stage amplifiers (HS-18-CNR-MDR50, Neuralynx) to a microdrive carrying eight tetrodes and an optic fiber (VersaDrive 8 Optical, Neuralynx) that was implanted in mice. Multi-unit spikes which passed 30-μV threshold were detected. All detected spikes were used to generate a peri-stimulus time histogram in relation to the onset of 3.7-ms light pulses delivered through the optic fiber. The presence of recording sites within/near the granule cell layer was confirmed in brain sections prepared after the completion of recording experiments.

QUANTIFICATION AND STATISTICAL ANALYSIS

Values are presented as mean ± s.e.m. in the text unless otherwise stated. Bar graphs, error bars, triangles in the graphs represents mean, s.e.m. and individual samples, respectively. Statistical analyses were performed in SPSS software (IBM). For independent sample t tests, we first performed Levene's test for the equality of variance. We performed Student's t tests when $p > 0.05$ for the Levene's test, and Welch's t test when $p < 0.05$. p values for two-tailed tests are presented.